ELSEVIER

Contents lists available at ScienceDirect

Journal of Membrane Science

journal homepage: www.elsevier.com/locate/memsci





Molecular insights into charged nanofiltration membranes: Structure, water transport, and water diffusion

Suwei Liu^a, Saahir Ganti-Agrawal^b, Sinan Keten^{a,c}, Richard M. Lueptow^{a,d,e,*}

- ^a Department of Mechanical Engineering, Northwestern University, Evanston, IL, USA
- ^b Department of Material Science and Engineering, Northwestern University, Evanston, IL, USA
- ^c Department of Civil and Environmental Engineering, Northwestern University, Evanston, IL, USA
- d Department of Chemical and Biological Engineering, Northwestern University, Evanston, IL, USA
- e The Northwestern Institute on Complex System (NICO), Northwestern University, Evanston, IL, USA

ARTICLE INFO

Keywords: Nanofiltration Molecular dynamics Polyamide film Membrane charge Water transport

ABSTRACT

While polyamide-based reverse osmosis (RO) and nanofiltration (NF) membranes are widely used for desalination and water purification, the influence of membrane porosity and charge on water transport remains to be fully understood at a molecular level. Here we use molecular dynamics (MD) to build 56 distinct piperazine-based NF membranes models, which cover a membrane density range of 0.78 g cm⁻³ to 1.08 g cm⁻³. These membrane models have various charge concentrations, corresponding to a pH range of 4–11. Results indicate that membrane charge is not monotonically correlated with the membrane density or the water transport. Instead, the water transport is mostly determined by the membrane's physical properties, specifically, the membrane density, with charged membrane end groups and counterions causing swelling of the membrane, which tends to increase flux. Additionally, the diffusion coefficient of water molecules within the membrane is strongly correlated with the membrane density. The diffusivity of water is independent of the transmembrane pressure, even under the large pressures employed in molecular simulations. Thus, the transmembrane pressure biases the direction of the random walk of water molecules through the membrane resulting in a water flux but does not alter their overall mobility within the membrane. These findings shed light on the relationship between membrane properties and water transport for charged membranes, as well as providing new insights into the structure of NF membranes at a molecular scale.

1. Introduction

Freshwater scarcity is an ever-present and growing threat worldwide as rapid industrialization, population growth, and climate change burden water resources that are already heavily utilized by industry, agriculture, and municipalities. One promising solution is using polyamide (PA) membrane systems for water purification. PA membranes consist of a thin active layer deposited on a porous substrate. This active layer has pores on the Ångstrom or nanometer scale that are responsible for the high rejection of undesired solutes while still passing water. Of the two main types of PA membranes, it is well-established that nanofiltration (NF) membranes are effective in removing large organic compounds [1-3], while reverse osmosis (RO) membranes have been used widely for ion removal due to their small effective pore sizes [4,5]. However, to address the pressing need for clean water and the worldwide energy crisis, NF membranes play a critical role as they reject divalent ions with significantly lower energy cost [6,7] than RO membranes. The challenge is predicting how interactions between ion

solutes and charged NF membrane's molecular structure alter the solute selectivity. These interactions are poorly understood, which prevents NF membranes from being used in situations that would benefit from their low energy usage or selective contaminant removal [8–10]. Understanding the interplay between pore size, molecular mobility, and charge is particularly important for NF membranes given that they tend to be more porous than RO membranes. Moreover, an important characteristic of NF membranes is that they are typically charged such that a fraction of carboxyl groups are deprotonated at a given pH value, which can affect the membrane transport characteristics. In this paper, we use MD simulations to explore how membrane charge affects the structure and water dynamics in NF membranes as a precursor to further study of how charged solutes interact with NF membranes.

Over the past two decades, a number of experimental studies [11–16] have been conducted to visualize and understand the microstructure of PA membranes, and theoretical studies [17,18] have correlated the PA membrane structure with its performance (ion selectivity and

^{*} Corresponding author at: Department of Mechanical Engineering, Northwestern University, Evanston, IL, USA. E-mail address: r-lueptow@northwestern.edu (R.M. Lueptow).

water flux). However, in order to uncover the membrane-water interactions at the fundamental atomic level, molecular dynamics (MD), a computational method based on modeling interactions of individual atoms, can provide exceptional insight. MD has been used previously to study RO membranes at the atomic scale [19-28], but these studies all focused on RO membranes of trimesoyl chloride (TMC) polymerized with m-phenylene diamine (MPD). While they shed light on the connection between MPD-based RO membrane structure and water transport, little effort has been dedicated to investigating NF membranes of TMC polymerized with piperazine (PIP). Moreover, atomistic scale simulations can provide information that is very difficult to obtain experimentally. For example, it is extremely challenging to measure the porosity and density of NF membranes since their active layers are usually less than 100 nm thick [29]. MD studies of NF membranes can easily provide density and pore size characterizations that can be used to connect transport observations and continuum models to atomic-scale interactions. Trajectories of water molecules as they diffuse through the membrane can be tracked, along with membrane dynamics including positions of charged groups and solutes, all with sub-picosecond resolution.

A recent experimental study has shown that the solution pH has an effect on PIP-based NF membranes in rejecting anions with different charge densities [30]. Thus, one would expect that enhancing membrane performance may depend on a molecular-scale understanding of the interactions between the feed water and the negatively-charged carboxyl groups of the membrane itself [31,32]. Different compositions and concentrations of feed solutes change the pH of the membrane environment. This directly affects the membrane charge interactions, influencing membrane porosity, ion selectivity, and water transport. However, most atomistic simulations of RO membranes have assumed that the membrane has zero net charge [20,22,26,27,33]. The few computational studies that account for the negative charge of the membrane [25,28] have only considered a single ionization state of the membrane, which would correspond to only a single pH value. Accurate modeling of the membrane structure at varying membrane charge concentrations corresponding to different pH values is needed to understand the effect of membrane charge on membrane nano-structure and its subsequent impact on water transport.

In spite of the technical challenges in characterizing NF membranes, several studies have shed light on certain properties of NF membranes. The active layer of NF membranes is typically produced through interfacial polymerization (IP) of PIP and TMC. As a result of this rapid IP process, the active layer thickness of NF membranes can be extremely thin, for example, measured to be 34 nm thick [34]. On the other hand, RO membranes, of which the active layer thickness is much thicker, for example, measured to be 141 \pm 56 nm [35]. The ultra-thin NF membrane active layer means that NF membranes can be operated at a significantly smaller transmembrane pressure during desalination, which is generally within 0.45-0.75 MPa [36] for NF membranes compared to 1.7-6.9 MPa for RO membranes [37]. In addition to the active layer thickness, other physical properties of NF membranes have been measured. Although density measurements of the active layer are difficult to obtain as it is challenging to separate the active layer from the support structure, the effective pore size of NF membranes can be relatively easily determined based on the rejection of solutes [38]. The pore size range for typical NF membranes is 0.3-5 nm, while that of RO membranes is 0.1-2 nm [39]. Combining the factors of active layer thickness and pore size, NF membranes can have 1.5-3 times more flux than RO membranes [40]. Thus, RO membranes have relatively thick active layers and a tight molecular structure, while NF membranes are thin and looser in structure. This actually makes NF membranes more amenable to study using MD methods than RO membranes, because larger areas of thin, loose NF membranes can be effectively modeled within reasonable computational constraints.

The objective of this study is to develop atomistic models of piperazine-based NF membranes in which varying pH conditions for the membrane can be simulated and use these membranes to consider the effect of membrane charge on physical and water transport properties of the membrane. The NF membrane models used in this study are constructed from PIP and TMC monomers, which is a simplified realization of the commercial nanofiltration membrane FilmTec™ NF270 produced by DuPont Water Solutions. We describe a virtual polymerization scheme to make realistic and distinct NF model membranes that can be characterized in terms of density and pore size, depending on the deprotonation state. We use both Equilibrium MD (EMD) simulations (no pressure gradient across the membrane) and Non-Equilibrium MD (NEMD) simulations (with a pressure gradient across the membrane) to explore water diffusion and advective transport at equilibrium conditions and under a pressure gradient at the molecular level. In this study, 56 distinct membrane realizations were constructed and 220 independent water transport simulations lasting 20 ns were conducted. This large number of samples enables robust quantitative analysis and illuminates the relationship between membrane properties and water transport performance.

2. Methods

2.1. Construction of all-atomistic membrane models

2.1.1. Neutral membrane models

The approach to generate neutral membrane models is shown in Fig. 1(a), which is a similar procedure to the one described previously [20]. PIP-based NF membranes are computationally constructed by allowing PIP and TMC monomers to move randomly within a simulation box using molecular dynamics and then letting amide bonds form heuristically when reactants are within a threshold distance. The approach does not attempt to reproduce the actual reactions and polymerization process but rather aims to reproduce membranes with realistic density and molecular structure.

Models for PIP, TMC, the amide-bonded oligomer after crosslinking, and the amide-bonded oligomer after hydrolysis are built using the general AMBER force field (GAFF) [41]. The topology and force field parameters for these compounds are obtained using semiempirical bond charge correction (AM1-BCC) available in AmberTools18 [42,43]. The fix "bond/react" command [44] in LAMMPS [45] is used to generate bonds between reacting molecules. Prior to the polymerization process, TMC and PIP monomers are randomly placed in a simulation box, which is 52 Å \times 52 Å in the x- and y-directions and 50–70 Å in the z-direction depending on the model (further discussed in Section 2.2). The x- and y-directions are periodic; the z-direction, which corresponds to the thickness of the membrane, is not. The monomer mixture first undergoes minimization, which finds the local energy minima for the atoms, and then 10 ps equilibration using the canonical ensemble (NVT, where the amount, N, volume, V, and temperature, T, are constant) with a timestep of 1 fs. The external temperature set at 300 K and the temperature damping parameter at 100 fs. The polymerization reaction occurs when the acyl chloride from TMC and the amine hydrogen atom from PIP are within a pre-defined distance indicated by the bracket between the two monomers in Fig. 1(a). After removing chloride and hydrogen atoms, an amide bond is formed between two monomers as shown in the first step in Fig. 1(a), followed by partial charge adjustment. After the first reaction, each molecule has additional sites that are available for further crosslinking. The polymerization process is self-limiting because the diffusion of monomers slows considerably as the polymerized clusters grow. Within the total duration of 200 ps of crosslinking, the bonding distance between two monomers is set to 3.5 Å for the first 40 ps and then increased to 5.0 Å for the remaining 160 ps to speed up the polymerization reactions. At each timestep, if new bonds are formed, a NVT equilibration is performed with the aforementioned settings for 10 ps in addition to the total duration of 200 ps of crosslinking.

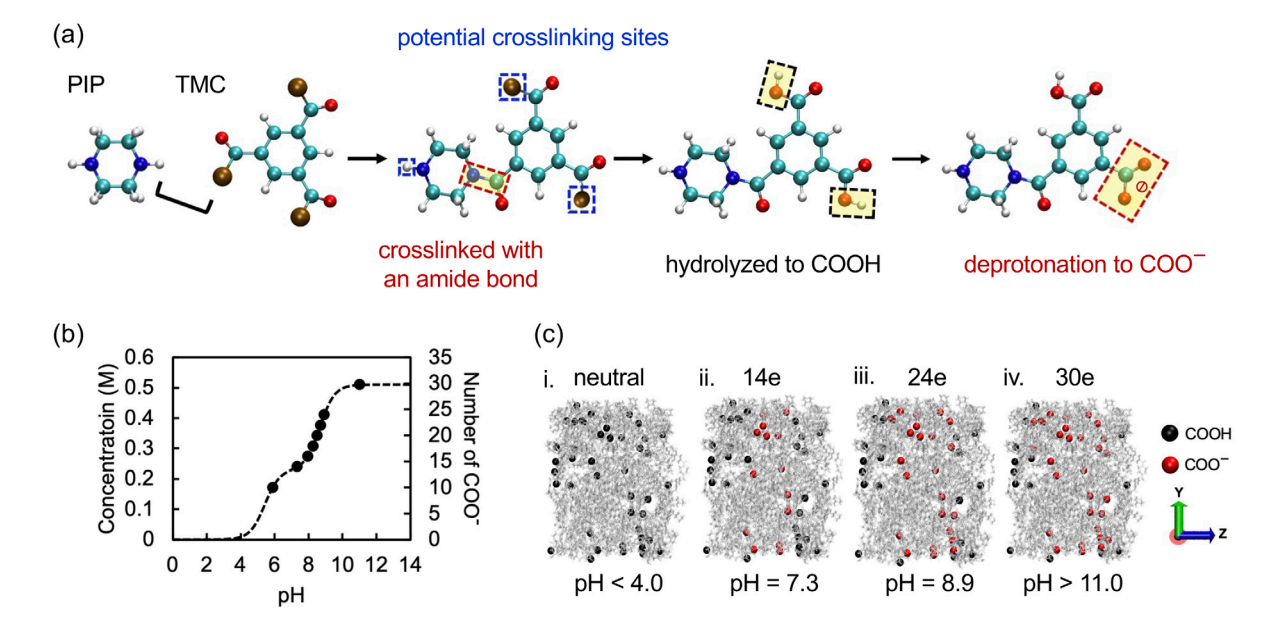


Fig. 1. (a) The monomers, crosslinked dimer, hydrolyzed dimer, and deprotonated dimer configurations, where blue, white, cyan, brown, and red beads represent N, H, C, Cl, and O respectively; (b) dependence of carboxylate molar concentration [46] (dashed curve, left vertical axis), and the number of carboxylate end groups in a membrane model of 97 nm³ (black circles, right vertical axis) as a function of pH for an ESNA-NF membrane; (c) i. neutral membrane with all protonated carboxyl groups (black), and ii.–iv. 14e, 24e and 30e charged membranes with carboxylate end groups (red) and protonated carboxyl groups (black). (Color online.).

At the end of each polymerization simulation, monomers that are not chemically bonded to the polymeric matrix are removed. Each unreacted acyl chloride atom is thereafter replaced by a hydroxyl group, resulting in a carboxyl group at the carbonyl site, which is equivalent to hydrolysis for an actual membrane, as shown in the second step of the polymerization process in Fig. 1(a), resulting in a neutrally charged membrane. For all the TMC-based segments containing carboxyl groups, the partial charges are re-adjusted manually according to the partial charge profiles parametrized by AmberTools18 [42,43] so that the final membrane models are uncharged.

After partial charge adjustment, an equilibration is conducted using the NAMD (Nanoscale Molecular Dynamics) simulation package [47] along with GAFF forcefields [41]. All neutral membranes are equilibrated in vacuum at 300 K, using a timestep of 1 fs at a constant pressure of 1 atm in the isothermal-isobaric (NPT) ensemble for 10 ns using a computational box size that is the same as the one used in the polymerization. Again periodic boundary conditions are used in the xand y-directions, while the z-direction is non-periodic to represent the finite thickness of the membrane model. The SHAKE algorithm [48] with a cutoff of the non-bonded potential of 9 Å is used to constrain the bond between each hydrogen and its mother atom. The Particle Mesh Ewald (PME) method [49] is used to compute full electrostatics with a grid spacing of 1 Å. Although a switching function for Lennard-Jones (LJ) potential is normally used in NAMD simulation program, we turn it off since we are using AMBER forcefields. Instead, the NAMD command "LJcorrection" [47] is used to correct the amount of lost long-range energy due to LJ potential cutoff settings.

2.1.2. Charged membrane models

When real membranes are in operation, the feed pH and pK_a determine the ionization state of carboxyl groups (COOH) within the membranes. However, it is difficult to simulate these effects, so instead we simply assume a pH and adjust the membrane charge to be consistent with that pH. The relationship between charge concentration and feed pH has been quantified for several types of water filtration membranes [16,46,50], but we are unaware of any reports on the specific relationship for PIP-based NF membranes that we consider here. To model charge concentration in the absence of this data, we assume that our PIP-based NF membranes follow a similar charge vs. pH

relationship as an ESNA-NF membrane. This is because ESNA-NF best matches FilmTec™ NF270 in terms of elemental composition [51,52] and isoelectric point [46,53]. Although ESNA-NF is based on MPD (fully aromatic) and FilmTec™ NF270 is based on PIP (semi-aromatic), neither MPD nor PIP has a significant effect on the pK_a of the acidic groups due to the spatial distance between COOH end groups and the amide bond. Furthermore, we focus on the results measured using Rutherford backscattering spectrometry because this technique is not constrained by specimen thickness, and therefore should be more accurate than X-ray photoelectron spectrometry [52]. Based on the parameters of ESNA-NF measured by Coronell, et al. [46], the correlation between charge concentration and pH is reproduced in Fig. 1(b). We arbitrarily select eight different charge concentrations, ranging from 0.17 M to 0.51 M, which corresponds to pH values of 5.9-11, noting that a neutral membrane corresponds to pH < 4.0. Given the volume of our membrane model (97 nm³), this concentration range corresponds to 10-30 negatively charged carboxylate end groups within the membrane.

Charged membranes are created by selectively deprotonating COOH groups, the sites of which are shown in Fig. 1(c)-i for one sample equilibrated neutral membrane. The locations of COOH in the membrane model depend on the final position of crosslinked TMC and the degree of crosslinking, which vary slightly from one membrane model to another. To construct charged NF membrane models, a certain number of carboxyl groups are deprotonated by removing their hydrogen atoms, shown as the last step in Fig. 1(a). The deprotonation sites are arbitrarily chosen but intentionally concentrated in the center of the membrane as shown in Fig. 1(c) ii-iv. The corresponding pH depends on the number of carboxylates. For instance, in Fig. 1(c)ii, 14 of 34 carboxyl groups are deprotonated (designated as "14e" for 14 negative charges) corresponding to pH = 7.3 for the 97 nm³ membrane, according to Fig. 1(b). To achieve higher pH, successively more carboxyl groups are deprotonated. After the hydrogen-removal process is finished, the partial charges of all the deprotonated TMC are re-adjusted according to the partial charge profiles parametrized by AmberTool1s8 [42,43] to match the membrane's negative charge level.

2.1.3. Membrane hydration

To hydrate a virtual polymeric membrane model, it is common to artificially insert water molecules into any of the voids present in the molecular structure of the membrane model, regardless of whether those voids are accessible to water through permeation [23,24]. By contrast, in order to mimic the hydration process in real membranes (in which voids inaccessible to water molecules will not be hydrated), we use simulations with no transmembrane pressure to let water diffuse into the membrane. The equilibrated dry membrane is placed between two water reservoirs. Each reservoir has the same x- and y-dimensions as the membrane, and the z-dimension is set to 30 Å, which is sufficiently large to contain enough water molecules for the membrane to be fully hydrated. Periodic boundary conditions are used in the xand y-directions (plane of membrane's cross-sectional surface) while z-direction is non-periodic. During the hydration process, each water reservoir is "sandwiched" between the membrane and a graphene sheet. The graphene sheets are built using the Nanotube Builder available in VMD (Visual Molecular Dynamics) [54] and parametrized using the AmberTools18 force field [41]. Each graphene sheet is merely used to model an impermeable surface, to which pressure is applied at the outer boundary of the reservoir.

The hydration process for neutral membranes requires simulations with two pressure settings. A pressure of 30 MPa is applied on both graphene sheets for 5 ns in order to quickly solvate the membrane, followed by a 40-ns equilibration-diffusion period with a pressure of 0.1 MPa on both sides. The NVT ensemble is used and water molecules are modeled using the TIP3P potential [55]. The system size in all directions is kept constant. The global thermostat, PME [49], SHAKE algorithm [48], and switching function settings are kept the same as previously used for equilibration of the membrane.

For charged membranes, the hydration step and membrane equilibration are combined. This is necessary because, when equilibrating the charged membrane models, sodium (Na⁺) counterions are added so that the overall net charge of the entire simulation system is zero. This ensures the long-range electrostatics are correctly computed. When assessing the feasibility of simulating a charged membrane and free counterions in vacuum, as is done with the equilibration of the base neutral membrane, we observe that the counterions infiltrate the membrane, and it contracts due to strong electrostatic interactions. Furthermore, these abnormally dense membranes have substantially reduced water uptake during hydration simulations, which alters the water transport in the membrane. Consequently, we do not follow the equilibration protocol used for neutral membranes (equilibration in vacuum, followed by hydration). Instead, we perform EMD simulations with both water and counterions in the reservoirs on either side of the membrane to simultaneously hydrate and equilibrate the charged membranes. Each charged membrane is placed between two identical reservoirs (membrane area and 30 Å in the z-direction), to which the same number of counterions are added, half on each side of the membrane, to balance the membrane charge. The parameters of the 6-12 LJ potentials for Na+ are extracted from Ref. [56]. Similar to the hydration setup of a neutral membrane, two simulations at different pressures with a total duration of 45 ns are performed. Using this approach, counterions diffuse into the membrane together with the water molecules.

2.2. Membrane models used in this study

To create realistic NF membrane models, we consider three different PIP:TMC monomer reactant ratios for the polymerization simulations. All of the PIP:TMC ratios are evaluated after polymerization (due to potential deletion of unreacted monomers) and the atom content after hydrolysis is analyzed to compare to an experimentally-derived PIP-based membrane. The atom content (C, O, N) and O/N ratio for different PIP:TMC ratios are listed in Table 1, along with measurements from a real PIP-based NF membrane [51]. Since the monomer ratio is within a narrow range of values, the elemental composition does not differ significantly. Although the O/N ratio and atom content measurements only approximately agree with the experimental membrane, a monomer ratio of 1.45 is used for all membrane models because it

Table 1
Membrane elemental composition for three monomer ratios compared to an experimental NF membrane. For MD models, each ratio is based on three different membrane realizations.

MD Models			Experiments [51]	
PIP:TMC	1.42 ± 0.005	1.45 ± 0.004	1.51 ± 0.000	N/A
O/N ratio	1.163 ± 0.005	1.100 ± 0.003	1.038 ± 0.065	1.14 ± 0.01
C (%)	70.51 ± 0.20	70.81 ± 0.01	70.95 ± 0.07	72.95 ± 0.25
O (%)	15.86 ± 0.25	15.29 ± 0.02	14.79 ± 0.08	14.40 ± 0.20
N (%)	13.63 ± 0.05	13.90 ± 0.02	$14.26~\pm~0.01$	12.65 ± 0.05

Table 2 Categories of simulated membranes and the number of PIP and TMC monomers for PIP:TMC = 1.45.

Group	Area (Ų)	PIP:TMC
small dense	52 × 52	332 : 228
large dense	74 × 74	671 : 463
small loose	52 × 52	332 : 228

renders the best compromise for the atom content profile of the MD model membranes to be similar to an actual membrane polymerized using PIP and TMC.

One of the challenges in performing MD simulations of membranes is that the membrane dimensions have to be small for computational efficiency. Since the membrane can only be a few to several nanometers in any dimension, major heterogeneities such as voids or dense regions may have a strong affect on subsequent measurements. In fact, experiments have demonstrated that the active layer of PA membranes has these sorts of heterogeneous features [16,57,58]. To visualize this, energy-filtered transmission electron microscopy and electron tomography have been used to reveal how nanoscale inhomogeneity within the active layer of RO membranes produces high- and lowflux regimes [34]. An advantage of the MD approach is that we can create membrane models with a wide range of densities by manipulating the computational polymerization process. This can be useful for considering how local heterogeneities can influence flux in largescale membranes. We are able to create membrane models with quite different densities by changing the monomer packing density prior to polymerization and the polymerization box size. To probe this effect in detail, we construct 21 neutral NF membrane models with different densities and membrane areas, which can be categorized into three groups: small-dense (12 models), large-dense (3 models), and smallloose (6 models), detailed in Table 2. Small/large refers to the area of the membrane and dense/loose refers to the polymeric nanostructure. Within either the small-dense or small-loose groups, different monomer packing densities and reaction box sizes (see Table S1) are used to build a variety of membrane models, aiming to cover a range of membrane densities. Reaction box sizes of a smaller extent in the z-direction result in more dense membranes. Additionally, we construct a set of membranes with twice the area of the small membranes to be sure that the membrane area does not affect the structural or water transport properties of the membrane. These large-dense membranes are not used in the charged membrane portion of this study.

2.3. Molecular dynamics simulations of water transport

The setup for water transport simulations is illustrated in Fig. 2 using the 14e membrane (corresponding to pH = 7.3) from the small-dense group as an example. The system consists of the hydrated membrane between two water reservoirs containing sodium counterions, bounded by two graphene sheets to apply pressure to force water through the membrane. For a charged-membrane system, the hydrated membrane section includes the equilibrated membrane, the water molecules that are absorbed within the membrane at the end of the EMD simulations at t=45 ns for hydration, and the sodium

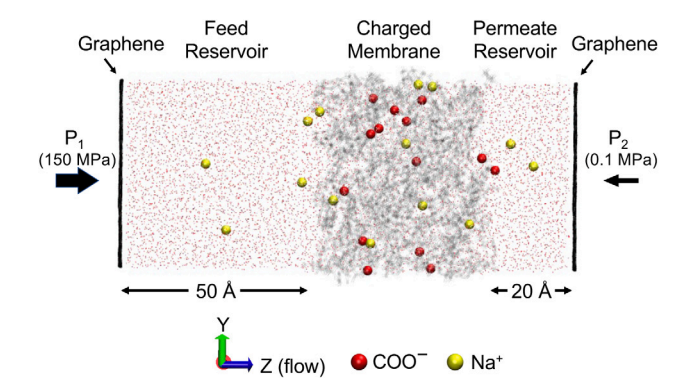


Fig. 2. NEMD simulation setup at t=0 ns for a 14e membrane from the small-dense group. Water molecules are red points (not related to the actual size), graphene sheets are black, membrane atoms are gray, the 14 carboxylate sites (corresponding to pH = 7.3) are labeled as red beads, and counterions are yellow beads. The membrane looks somewhat different from the one in **Fig. 1c-(ii)** because the structure changed slightly after hydration and equilibration. (Color online.).

counterions inside the membrane. To assure that the entire system is neutral, additional counterions are added to either water reservoir so that the counterions on both sides of the membrane center in the *z*-direction are as close to equal as possible. For a neutral-membrane system, the hydrated membrane section consists of the equilibrated membrane and the absorbed water molecules with no counterions.

The dimensions of the feed and the permeate reservoirs match the dimensions of the membrane in the x- and y-directions with periodic boundary conditions. For dense membrane systems, the feed reservoir is 50 Å in z-direction, while for loose ones it is increased to 60 Å to ensure an adequate water supply at a reasonable computational cost. The permeate reservoir is 20 Å in z-direction for all systems, which is adequate to prevent any substantial interactions between the membrane and the graphene without requiring excessive computational resources. A pressure of 150 MPa is applied to the left graphene sheet while a back pressure of 0.1 MPa is applied to the right one. This pressure difference mimics the actual filtration process, although the pressure used is two orders of magnitude larger than a typical NF membrane operating pressure [29]. This is necessary because MD simulations require much higher operating pressures in order to observe significant transport on nanosecond timescales [27]. We will show later that the resulting flux is consistent with that typically measured for NF membranes at normal operating pressures.

The system size in all directions is kept constant throughout the entire NEMD simulation. To allow the membrane to dynamically evolve during water transport without being displaced due to the large pressure difference, roughly 10% of the atoms in the y-z plane at the periodic boundaries of the membrane are fixed in space (see Fig. S1 in the supplementary material). To assure repeatability, four NEMD simulations lasting 20 ns are performed for each membrane model, starting with the same initial configuration. The global thermostat, PME [49], SHAKE algorithm [48], and switching function settings are kept the same as previously indicated.

3. Results

3.1. Neutral NF membrane structure

In order to characterize the membrane and provide a basis for comparing to other membrane properties, we determine the membrane density and measure its water content after membrane models are sufficiently hydrated and equilibrated. Fig. 3 shows the density profiles (the polymeric membrane density and the corresponding water content) for two neutral membrane examples, the neutral dense and the neutral loose. The density profiles show that the membranes have

an active dense portion that we refer to as an "active layer", which corresponds to the densest region of the membrane, excluding the looser, low-density polymeric structures at the surfaces. The thickness of the active layer is 36 Å for the dense membrane and 38 Å for the loose based on the concept of a Gibbs Dividing Surface [59]. This is roughly 10 times thinner than a typical PIP-based NF membrane such as FilmTec™ NF270, which has an active layer thickness of about 34 nm [29]. A thinner membrane is necessary for MD studies in order to observe statistically meaningful results for simulations with physical time durations measured in nanoseconds. Nevertheless, we will show shortly that water flux studies for the model membranes used here provide realistic results when accounting for membrane thickness.

Returning to the membrane density itself, the polymeric densities of the active layer after hydration, ρ_M (membrane-only, the mass of water is not included) are about 1.05 $~{\rm g\,cm^{-3}}$ and 0.81 $~{\rm g\,cm^{-3}}$ for dense and loose membranes, respectively. The standard error bars over the 4 ns time averages are generally the same size as the data markers in Fig. 3. The uniformity of the water wt% across the thickness of the membrane demonstrates that the membrane models are fully saturated with water at the end of the equilibration run.

It is difficult to compare the density of the membrane models to actual membranes. We have found no measurements of NF membrane density in the literature, most likely because physical PIP-based NF membranes have active layer thicknesses less than 100 nm, so that experimentally isolating and measuring the density of the active layer is quite difficult. As a result, we compare membrane density results to those of RO membranes, which are also polyamide membranes. Compared to RO membranes, NF membranes can have comparable or larger pores, which result in lower selectivity for small molecules, due to the size exclusion effect [38]. Therefore, NF membranes are expected to have a lower density within the active layer. In experiments, RO membranes have ρ_M in the range of 0.86–1.24 g cm⁻³ [34,60,61], and previous MD studies have revealed ρ_{M} for RO membranes to be 1.10 g cm^{-3} [21,22,27]. Our NF membrane models are on the lower side of the experimental measurements of RO membranes and have smaller densities compared to the computational RO membrane models, which is expected for membranes with a looser structure [38].

In the aforementioned studies, the density of the active layer in an RO membrane is usually reported as the total hydrated density ρ_{tot} (membrane plus water). In our models, ρ_{tot} of the "active" portion is $1.29~{\rm g\,cm^{-3}}$ for the dense sample and $1.24~{\rm g\,cm^{-3}}$ for the loose one. While ρ_{tot} for the loose membrane is only 4% less than the dense one, ρ_M of the loose membrane is 22% less than the dense one. The reason for this is that the weight percent of the hydrating water is 90% greater in the loose sample than the dense one, thereby obscuring the fairly large difference in the densities of the membranes alone. As a result, ρ_M will be used in this study instead of ρ_{tot} so that the physical differences between the membrane models themselves are clearly quantified.

In addition to analyzing membrane density, MD simulations provide the advantage of being able to measure the membrane porosity at the Ångström-scale. While the membrane does not contain straight, cylindrical channels, quantification of membrane porosity provides critical information about the local nanostructure. The pore size distribution (*PSD*) is characterized using PoreBlazer v4.0 [62] through a geometric method that determines the total free volume and the pore size distribution given a spherical "probe" of a particular size. In order to capture the membrane porosity with a high resolution, we use a probe size of 0.25 Å. This gives us a resolution that matches or exceeds atomic force microscope (AFM) measurements, which use 0.30 Å and 0.66 Å pixel sizes when imaging PIP-based NF membranes [63]. Moreover, AFM measurements cannot probe the interior porosity of the membrane, which is possible for simulated membranes.

Fig. 4 shows the PSD curves (in the form of a probability density function) for all neutral membrane models, where each curve represents an independent membrane realization. The three types of membranes have generally similar PSD curves with pores ranging from

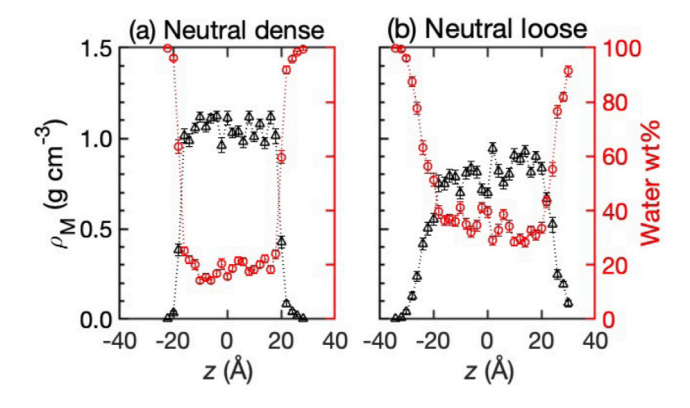


Fig. 3. Membrane density, ρ_M (left vertical axis) and water wt% enclosed in the membrane (right vertical axis) calculated and averaged over 2000 time instants separated by 2 ps during the last 4 ns of the equilibration. The data points are calculated for a 2 Å thick slice across the x, y-extent of the membrane at z-locations spaced 2 Å apart: (a) neutral-dense, and (b) neutral-loose membranes. (Color online.).

the probe size resolution of 0.25 Å up to about 6 Å for the dense membranes and even larger values for the loose membranes. The peaks in the PSD curves for all membranes are located at around 3 Å, which may correspond to the "network pores" formed by crosslinking within a given polymer chain or aggregate [66]. The vertical shaded regions in Fig. 4 indicate the range of water molecule diameters, from 2.8 Å, the Coulombic diameter, to 3.4 Å, the van der Waals (vdW) diameter [64,65]. Since the size of a solvating water molecule is best characterized by the Coulombic diameter when interacting with polar atoms, and the vdW diameter when interacting with nonpolar atoms, this range provides a good estimate of water molecule size within the membrane. Clearly, peaks in the PSD for all three membrane models roughly coincide with the size of water molecules. Water molecules are unlikely to pass through pores smaller than this size.

In small dense membranes (Fig. 4(a)), the maximum pore diameter ranges from 5.8 Å to 7.5 Å for different membrane models, suggesting that there are distinguishable variations in polymeric structure resulting from different polymerization setups (Table S1). On the other hand, the PSD curves for the large dense models shown in Fig. 4(b) are very similar to each other because of identical polymerization setups (Table S1). Unlike the dense membranes (Fig. 4(a, b)), loose membranes have substantially more pores with diameters greater than 6 Å and more pore size variations between models (Fig. 4(c)). The increased prevalence of large pores in the distribution may indicate the presence of "aggregate pores", which result from the open spaces that lie in between polymer aggregates [66]. The largest values for pore diameters of loose membranes range from 7 Å to 12 Å, which is in the range of aggregate pore sizes [66].

The results in Fig. 4 verify that manipulating initial crosslinking configurations can produce membrane models with distinct structures, as is desired here so the dependence of transport properties on membrane structure can be assessed. While the membrane models are distinct, each one is large enough so that it is not dominated by a single feature, such as the presence of a particular pore or channel, noting that the PSD curves are remarkably consistent within each category (dense or loose).

The effective pore diameter of NF membranes has been reported to be 7.80 Å and 8.96 Å in previous experimental studies [67,68], estimated from the size of permeated solutes. In an alternative approach, the mean pore diameter measured by AFM at the membrane surface has been found to be 3.10 \pm 0.66 Å for FilmTec^{∞} NF200, another commercial NF membrane type produced by DuPont Water Solutions with smaller mean pore diameter, and 7.1 \pm 1.4 Å for FilmTec^{∞} NF270 membranes [63]. Since the range of pore sizes indicated in Fig. 4 is consistent with these measurements of pore sizes in physical membranes, we conclude that the membrane models resemble real PIP-based NF membranes. Having a range of densities and pore sizes for

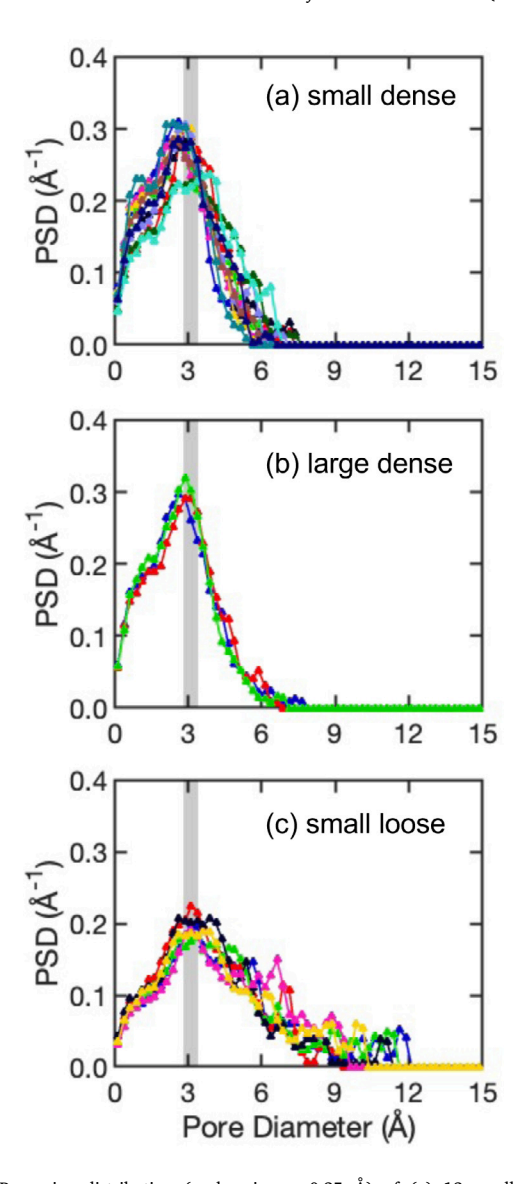


Fig. 4. Pore size distribution (probe size = 0.25 Å) of (a) 12 small-dense, (b) 3 large-dense, and (c) 6 small-loose neutral membrane models shown in different colors averaged over 10 time instants separated by 0.4 ns during the last 4 ns of the equilibration. The shaded region indicates the diameter range of a water molecule [64,65]. (Color online.).

the different membrane models enables us to investigate correlations between membrane structures and transport properties. Of course, further experimental studies on physical PIP-based NF membranes using techniques like positron annihilation spectroscopy would be helpful in providing more accurate estimates of pore sizes to which virtual membranes can be compared.

The correlation between membrane density and mean pore diameter for neutral membrane models is shown in Fig. 5. The two membrane categories, dense and loose, which results from different polymerization setups, occupy distinct density and pore diameter regions in the figure. The gap between the dense and loose membrane measurements occurs because the virtual polymerization used here is a complex stochastic process that could not be precisely controlled to produce a membrane model with a specific density. (This gap will be addressed again later in this paper.) Overall, the density decreases as the mean pore diameter increases, and the range of mean pore diameters for the model membranes straddles the diameter of a water molecule (2.8 Å to 3.4 Å [64,65]), which is again indicated by a shaded area. Although the mode pore size of the PSD in Fig. 4 for all membranes is approximately

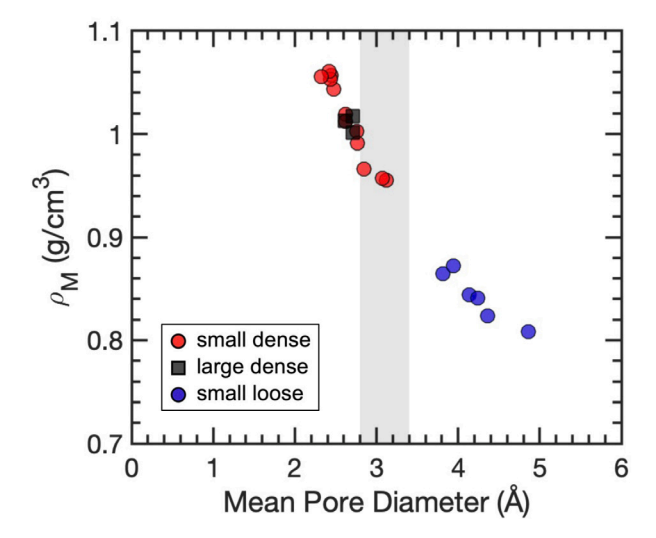


Fig. 5. Membrane density, ρ_M , as a function of mean pore diameter for small-dense (red circles), large-dense (black squares), and small-loose (blue circles) membranes, averaged over 10 time instants separated by 0.4 ns during the last 4 ns of the equilibration. The standard error bars are generally the same size as the markers or smaller, so they are omitted for clarity. The shaded region indicates the diameter range of a water molecule [64,65]. (Color online.).

equal to the diameter of a water molecule, the mean pore size in some dense membranes considered here is less than the size of a water molecule. As is evident in Fig. 4(a, b), the majority of pores in dense membranes are smaller than a water molecule. On the other hand, the mean pore diameters in loose membranes are greater than 3.4 Å, because the majority of pores in loose membranes are larger than a water molecule (Fig. 4(c)).

The mean pore size and pore size distribution only reveal the overall porosity in the membrane. To examine the volumetric porosity based on the size of a water molecule, we define the free space within the membrane that can occupy at least one water molecule as the free volume. Shown in Fig. 6(a), the free volume is measured using PoreBlazer v4.0 [62] with two probe sizes, corresponding to the Coulombic diameter (2.8 Å) and the vdW diameter (3.4 Å) [65] of a water molecule. The total free volume is normalized by the total membrane volume (periodic area times the distance between the Gibbs dividing surfaces) to produce a percentage value. It is evident that the free volume decreases linearly with increasing ρ_M regardless of the probe size as shown in Fig. 6(a), with the data for a 3.4 Å probe shifted vertically downward from that for a 2.8 Å probe, as would be expected. We also performed the free volume analysis with a probe size of 3.1 Å, the average of the Coulombic and vdW diameters of a water molecule. The results derived from a 3.1 Å probe lie between the ones calculated with 2.8 Å and 3.4 Å probes (data points omitted in Fig. 6(a) for clarity).

More important than the free volume is the percolated free volume, shown in Fig. 6(b), which quantifies the connected free space that water can travel from one side of the Gibbs dividing surface to the other. The percolated free volume for each membrane is less than its free volume at the same probe size, which indicates that some voids do not facilitate water transport. Furthermore, when considering all the cases here, the percolated free volume does not exhibit a clear linear relationship with ρ_M for the entire set of data. In fact, many of the dense membranes have zero percolated free volume at high values of ρ_M , suggesting that few water molecules can pass through these membranes even though the free volume itself is non-zero. Nevertheless, as will be shown later, these membranes have non-zero water flux indicating that thermal vibrations and collisions of water molecules with the membrane result in a dynamic pore structure [27] that allows some water molecules to pass through the membrane, although this

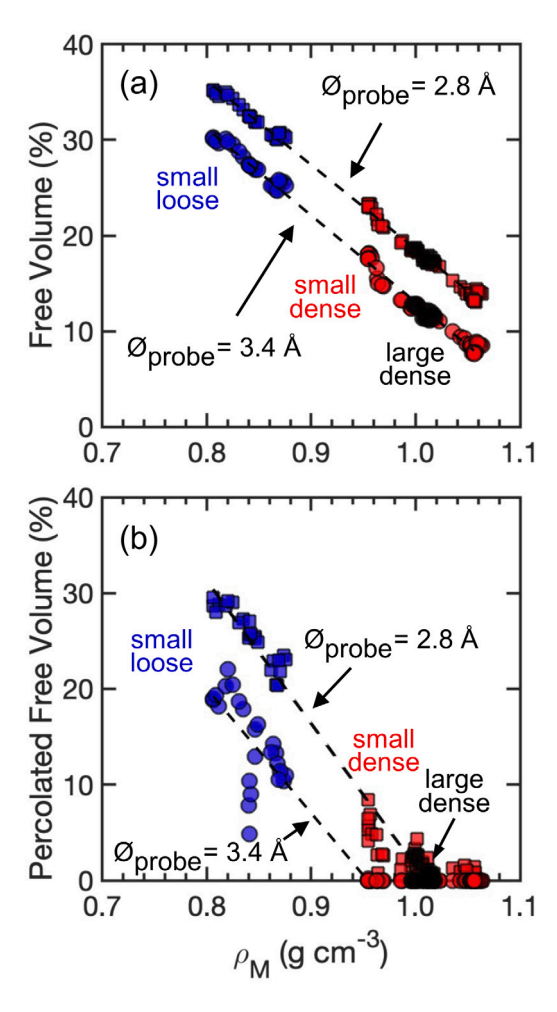


Fig. 6. (a) Free volume and (b) percolated free volume as a function of ρ_M , both calculated with probe diameters of 2.8 Å and 3.4 Å. All measurements of small-dense (red), large-dense (black), and small-loose (blue) membranes are based on 4 replicate NEMD simulations for each membrane model. Measurements are averaged over 10 time instants separated by 2 ns during the 20 ns NEMD simulation for each trial. Dashed lines are least squares fits to the data for each probe size and in (b) only non-zero percolated free volume data points are used for fitting. (Color online.).

is not necessarily reflected in the 10 time instants used to determine the percolated free volume. Moreover, including only data points for non-zero percolated free volume allows an approximately linear fit to the data, although the scatter is much greater than in Fig. 6(a). We also perform the percolated free volume analysis with a 3.1 Å probe and the corresponding results lie between the ones calculated with 2.8 Å and 3.4 Å for the small-loose membranes. For dense membranes, the percolated volume measured with a 3.1 Å probe is essentially zero, similar to the results for a 3.4 Å probe. In the remainder of this paper, we will use the membrane density to quantify the physical structure of the membrane, since it is a quantity that is more readily interpreted at the macroscale and avoids the complexity arising from determining the appropriate probe size.

3.2. Water flux in neutral NF membranes

Measuring the water flux allows us to understand how the physical property differences (density, pore size, percolated free volume, etc.) between membrane models are reflected in the water transport behavior. At the molecular level considered here, it is the easiest to measure the net change in the number of water molecules in the permeate reservoir from the beginning to the end of the simulation. The

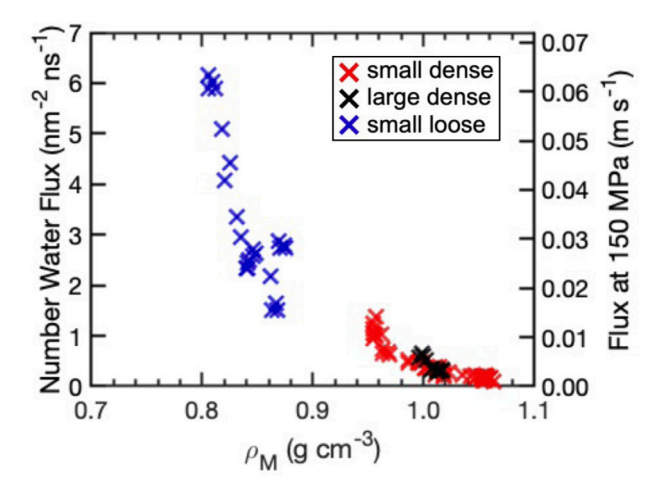


Fig. 7. Flux as a function of ρ_M for all small-dense (red), large-dense (black), and small-loose (blue) membranes. All measurements are based on 4 replicate NEMD simulations for each membrane model. (Color online.).

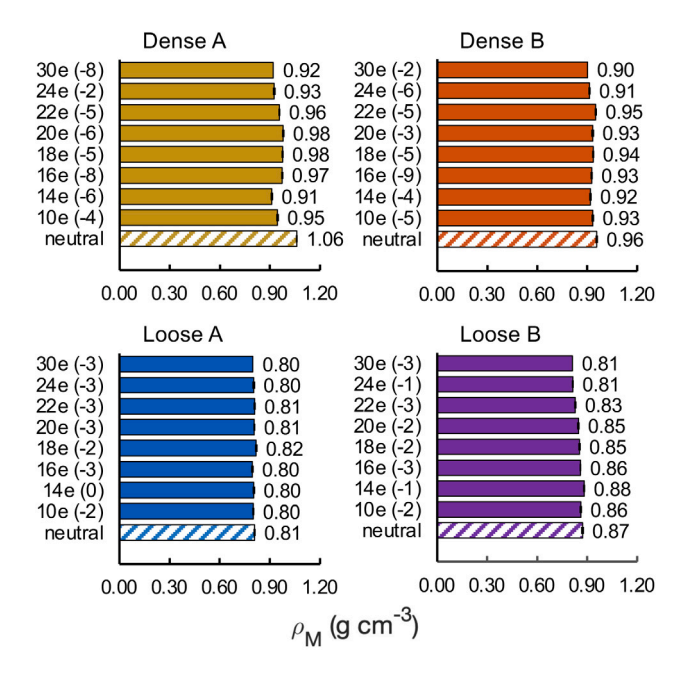


Fig. 8. ρ_M of neutral and corresponding charged membranes, averaged over the last 4 ns of the equilibration with a sampling frequency of 2 ps. The standard deviation is indicated by the error bars (barely visible because they are so small). Membrane net charge accounting for counterions inside each membrane is in parentheses. (Color online.).

water flux is obtained by normalizing the number of permeated water molecules by the simulation time (20 ns) and the membrane surface area (27 nm² for small membranes and 55 nm² for large membranes). This number water flux (nm $^{-2}$ ns $^{-1}$) can be converted to macroscale flux (m s $^{-1}$) by using the molar volume of water to calculate the flux as a volumetric flow rate per unit area.

The number water flux is shown in Fig. 7 as a function of ρ_M . Since the percolated free volume decreases with increasing ρ_M (Fig. 6(b)), flux also decreases as ρ_M increases. Although the decrease is monotonic, the dependence of the flux on the ρ_M is quite different for dense and loose membranes. For loose membranes, the flux is quite large compared to the densest membranes, where the flux is almost negligible (0.1 nm⁻² ns⁻¹), since these dense membranes lack enough percolated free volume to facilitate substantial water transport. Loose membranes have much larger percolated free volume, which greatly

facilitates water transport. Moreover, the results for flux and percolated free volume based on different probe sizes (Fig. 6(b)) also suggest that water molecules may be transported under two different conditions. The first is through the continuously connected channels, which are quantified by the percolated free volume. The other is "hopping" or "jumping" from one pore to another [27,69,70] even when the percolated free volume is essentially zero. Since the membrane nanostructure is in constant motion due to thermal vibrations and collisions with water molecules, pore dimensions are dynamic [27,71]. Thus, water molecules can "hop" from one pore to another as the pore structure changes, thereby accounting for a finite number flux of water molecules at large ρ_M even with zero percolated free volume.

At this point, it is useful to compare the number water flux in these virtual membrane models to the water flux in physical membranes. The fluxes for the virtual membranes in Fig. 7 span from 0.001 m s⁻¹ to 0.06 m s⁻¹ at 150 MPa (right vertical axis in Fig. 7). The flux measurements of commercial PIP-based NF membranes range from 7 to 13 liter m⁻² hr⁻¹ bar⁻¹ [67,72]. Accounting for the operational pressure difference and the active thickness difference between our membrane models (4 nm) and commercial NF membranes (34 nm [29]), the experimental flux values for commercial membranes are equivalent to a flux range of 0.024 m s⁻¹ to 0.046 m s⁻¹ at 150 MPa, consistent with what we measure here (Fig. 7). This further demonstrates that the virtual NF membranes studied here are physically representative of actual PIP-based NF membranes.

3.3. Membrane charge effect on structure and water transport

When NF membranes are used for water filtration, functional groups in the membrane structure can be deprotonated depending on the feed pH such that the membrane becomes charged [16,29,35,46,50]. We are interested in how the membrane charge affects the membrane structure (ρ_M) and water transport behavior. One advantage of MD simulations is that we can precisely control the charge concentration and directly compare a membrane sample in the neutral state versus the one with varying degrees of protonation.

To examine the effect of charge on the membrane density, we consider two neutral membrane examples (labeled A and B) from the small dense and small loose groups, respectively. It is from these four neutral membranes (Dense A, Dense B, Loose A, Loose B) that all charged membranes are derived. Each neutral membrane is used to generate 8 differently charged membranes by incrementally deprotonating random carboxylic groups, where the number of carboxylates increases from 10 to 30, corresponding to pH values 5.9–11 according to Fig. 1(b).

The membrane density ρ_M for the charged membrane models and the corresponding neutral membranes are summarized in Fig. 8. For each of the four cases, charged groups are progressively added to the neutral membrane (from zero charged groups for the neutral membrane up to 30 charged groups). Each resultant charged membrane is reequilibrated as described earlier. Note that ρ_M is averaged over the last 4 ns of equilibration for the active layer between the Gibbs dividing surfaces, and the small error bars indicate each charged membrane is adequately equilibrated after charge application. Comparing the density of the neutral membranes to the charged ones, it is evident that adding charge to the membrane slightly reduces ρ_M , suggesting that the membrane swells slightly as charge (or pH) increases in most cases. This density reduction is most evident for the Dense A case where ρ_M decreases by 12% on average compared to its base neutral membrane. This can be explained by the rearrangement of local polymer chains after charge application. More specifically, when certain carboxylic sites are deprotonated to negatively charged end groups, they experience strong electrostatic interactions that tend to swell the membrane as they undergo the re-equilibration process. Hence, charge application, in this case, leads to looser structures. For instance, the overall thickness of a neutral membrane from the Dense A group is 48 Å (measured from edge to edge), whereas the overall thickness

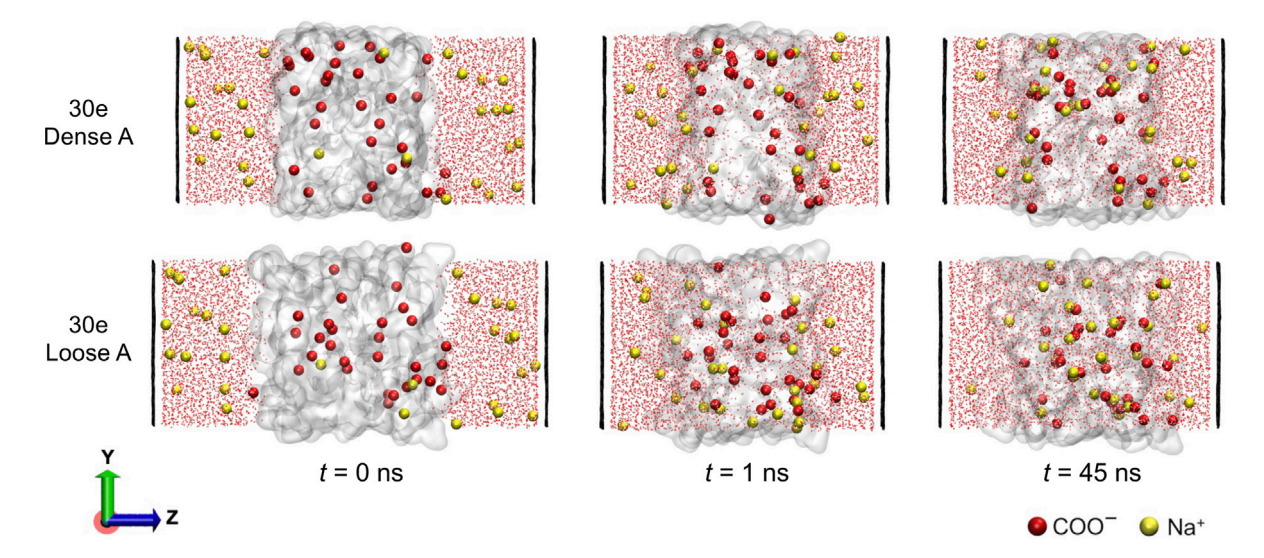


Fig. 9. Snapshots of EMD simulations of 30e membrane from Dense A group (top) and 30e membrane from Loose A group (bottom) at t = 0 ns, 1 ns and 45 ns. The pressure on both sides is 30 MPa for t = 0.5 ns to solvate the membrane and then set to 0.1 MPa for t = 5.45 ns to allow for normal diffusion. Water molecules are red dots, graphene sheets are black, and membranes are gray. (Color online.).

of a 30e membrane derived from this neutral membrane is 64 Å, although the active portion thickness of these two membranes are very similar, measured to be 32 Å (neutral membrane) and 34 Å (30e membrane). The swelling behavior is less pronounced in the other three membrane groups as the density variation is less than 4% for Dense B and Loose B, and only 0.6% for Loose A. When the base neutral membrane is already relatively loose, the deprotonated structure does not vary significantly from its neutral state, apparently because the additional free space between polymer chains results in weaker charge interactions. Consequently, the feed pH affects membrane structure more significantly when the membrane is in the high-density range.

From Fig. 8, it is evident that the trend between membrane density and charge concentration (the number of carboxylates) is neither monotonic within each membrane group nor consistent across all membrane groups. Apparently, the variation in the distribution of COOH end groups, which is different within each base neutral membrane, gives rise to the randomness observed in the deprotonated membrane structures. We also conjecture that the counterions, some of which end up inside membrane after equilibration as shown in Fig. 2, could play a role. To examine this, we consider the membrane net charge by combining the charge of carboxylates and sodium cations within each membrane, displayed in the parentheses for each membrane model in Fig. 8. The loose membranes have lower negative net charge and a narrower range of charge than the dense membranes, most likely because counterions can access the free space more easily. To demonstrate this, Fig. 9 shows results for 5 ns of fast solvation with a pressure of 30 MPa on both sides of the membrane followed by 40 ns with a pressure of 0.1 MPa on both sides. Both water molecules and sodium counterions can move into both Dense A 30e and Loose A 30e membrane models within 1 ns due to the interaction between negatively charged carboxylate end groups and positively charged sodium counterions. However, more sodium counterions move into the Loose A 30e membrane within 1 ns, and there are more sodium ions inside Loose A 30e membrane at the end of the EMD simulation. Additionally, sodium counterions are more likely to be found close to the carboxylates in the Loose A 30e membrane. Video V1 in the supplementary material shows the dynamics of the sodium counterions entering the membrane. This result persists even under high transmembrane pressure. Video V2 in the supplementary material shows the NEMD simulations of Dense A 30e and Loose A 30e membrane models. Despite the high transmembrane pressure used in these simulations (150 MPa), sodium ions inside the membranes are still very likely to be found in the vicinity of carboxylate

groups. However, there seems to be no meaningful correlation between membrane density and net charge either within one membrane case or across all four cases (see Fig. S2 in the supplementary material). Hence, the membrane density, while affected by the charge, does not seem to have a consistent dependence on either the nominal membrane charge or the net charge.

To consider the effect of membrane charge on water transport, the number water flux is plotted against membrane density for all charged membranes and their corresponding neutral base membranes in Fig. 10(a). The number water flux decreases as ρ_M increases regardless of the charge on the membrane, which is indicated by the type of symbol. That the number water flux does not have a clear relationship with membrane charge is consistent with the result in Fig. 8 where ρ_M has only a minor correlation with the membrane charge. Instead, the number water flux depends primarily on the membrane density for charged membranes just as it does for uncharged membranes (Fig. 7). However, there is a distinction between charged and uncharged membranes, illustrated by the curves fitted with power law functions separately through the data for the charged membranes and the neutral base membranes. The data points for the charged membranes shift slightly to the left compared to the neutral base membranes. For the two dense membrane sets, membrane charge leads to a looser structure, which, in turn, increases flux in the dense membranes (data points shift leftward and upward from the corresponding neutral membranes). A similar result occurs for several of the charged Loose B membranes, particularly for highly charged membranes. But for other charged Loose B membranes, particularly those at a lower charge, the membrane density remains mostly unchanged and the number water flux shifts downward. Likewise, for Loose A membranes, charge does not affect the membrane density at all but reduces the number water flux. This could possibly be attributed to the counterions in the membrane interacting with water molecules locally, but we have not tested this. In dense membranes, local charge effects are less important as membrane structure likely plays a bigger role in controlling flux.

Note that the initial simulation results for two membrane models, 20e from Loose A group and 18e from Loose B group, deviate from the charged membrane trendline. To investigate this, we simulate two more cases of the 18e membrane from Loose B group, the initial flux results for which are above the neutral trendline (purple upright triangles). In one case, the same initial configuration as the previous 18e membrane before equilibration is used, but a new equilibration run is performed. For the other case, the positions of 16 carboxylates in the membrane

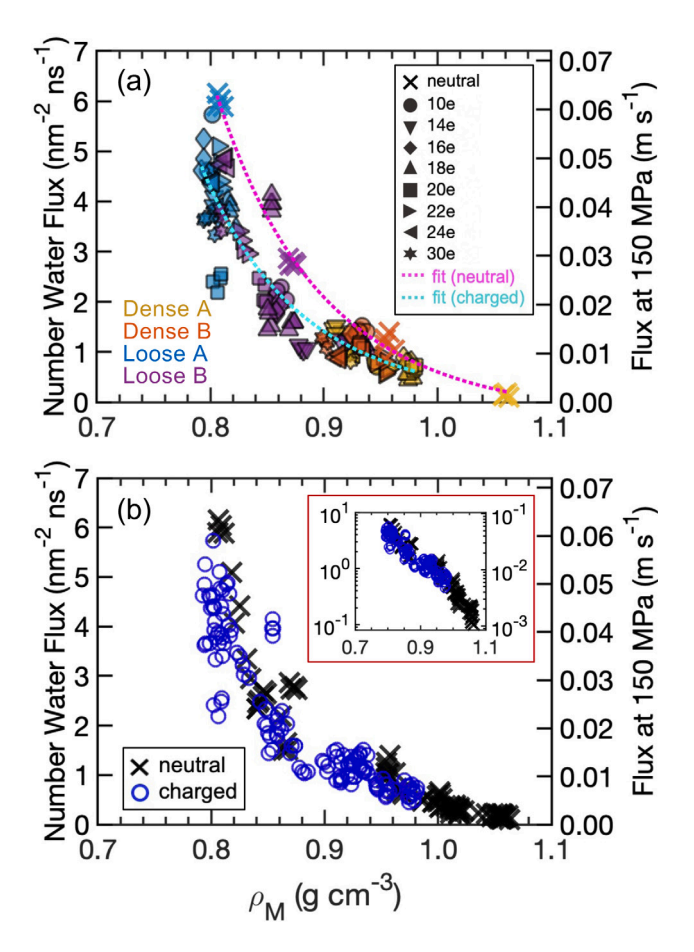


Fig. 10. (a) Flux as a function of membrane density ρ_M among 8 differently charged membranes (4 replicate runs per model) based on four corresponding neutral base membranes (152 total simulations). The dashed curves fitted with power functions are drawn to guide the eye. (b) Flux as a function of neutral (×) and charged (\bigcirc) membrane models (220 simulations) used in the study; the inset shows flux measurements on a semi-log scale. (Color online.).

remain the same, but the two additional carboxylates are located closer to the permeate reservoir, different from their previous positions. The same protocols for equilibration and water transport simulations are used to perform 4 trials per membrane (8 simulations in total). The new results for the 18e membrane (purple upright triangles) move vertically down from the original ones, falling back onto the charged membrane trendline.

To understand the difference between these 18e membranes, consider two 18e membrane samples, where one sample is from the original model and the other sample has the same pre-equilibrated structure as the original one but undergoes a new equilibration run. Since these two samples have the same initial structures before equilibration, the structural difference within the two samples during NEMD simulations can be indicated by the time-averaged distance between carboxylate groups in the two samples. Snapshots of 7 out of 18 carboxylate group pairs that change their location by more than 6 Å from one equilibration to the other are shown in Fig. 11, highlighted in matching colors. The arrow direction indicates how the carboxylate groups shift from the original 18e membrane model to the newly equilibrated one. The carboxylate location shift does not have a clear trend; the shifts in location seem to be random in direction and magnitude. That the distribution of carboxylates differs from one membrane sample to the other indicates that the arrangement of chains within the membrane can change, depending on the equilibration. The large difference in flux values, 4.1 nm⁻² ns⁻¹ and 1.6 nm⁻² ns⁻¹ with only a 2% change in membrane density indicates that the nanostructure

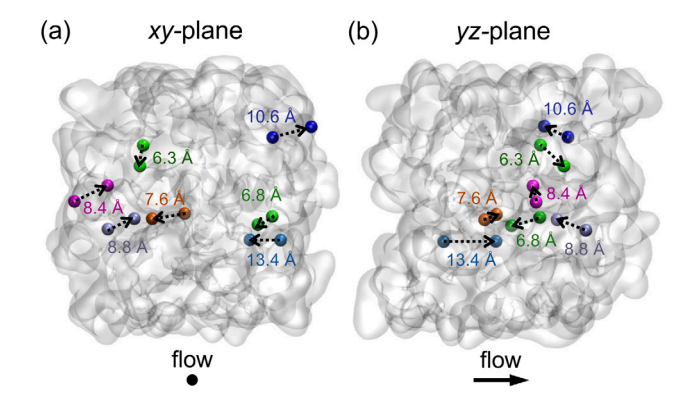


Fig. 11. Snapshots of 7 carboxylate group pairs exhibiting a shift larger than 6 Å, arrows pointing from an original 18e membrane (higher flux above the charged membrane trendline in Fig. 10(a)) to a newly equilibrated 18e model (lower flux falling on the charged membrane trendline). The distance is averaged throughout the entire NEMD simulation. The membrane structures are gray. (Color online.).

of the two membranes is quite different. To demonstrate this, video V3 in the supplementary material shows how different the permeated water movements are for the two 18e membrane models with different equilibration runs. For the membrane with a higher flux, water molecules pass quite easily through the lower one-third of the membrane, while for the other membrane with a lower flux fewer water molecules pass through the entire membrane, particularly in the lower one-third. This suggests a channel in the high flux membrane that does not exist in the low flux membrane, simply as a results of randomness in the equilibration. This discrepancy found in our membrane models coincides with the heterogeneity that is observed in physical PA membranes [34]. Most PA membranes are manufactured using interfacial polymerization, which is too fast to be in equilibrium [73]. Hence, in real membranes, there could be substantial heterogeneity [34] such as distinct loose and dense regions. Since spatial heterogeneity is hard to simulate given the small size of our membrane models due to computational constraints, we use a wide range of individual models (different membrane densities and charges for the 152 simulations represented in Fig. 10(a)) to extract the general trends that may be hidden in noisy results due to the membrane heterogeneity.

In spite of substantial variations in membrane size, membrane structure, and membrane charge, there is a remarkably consistent relationship between water flux and membrane density, as shown in Fig. 10(b). Further note that the flux values measured for charged membranes overlay those for uncharged membranes. In fact, charged membranes fill the gap at membrane densities of $\rho_M \approx 0.9 \text{ g cm}^{-3}$ observed in the neutral cases (Fig. 6(b)), resulting in a continuous variation in ρ_M and clear monotonic dependence of the number water flux on membrane density. Thus, although there is a slight dependence of membrane flux on charge, evident in Fig. 10(a), the flux is most strongly dependent on membrane density. Furthermore, when the same data is replotted on a semi-log scale (inset in Fig. 10(b)), there is a clear linear relation for $ho_M < 1.05~{
m g\,cm^{-3}},$ while the water flux decreases sharply for $\rho_M \geqslant 1.05 \text{ g cm}^{-3}$. This suggests that there exists a membrane density, above which water transport does not occur at all. This critical density of $\rho_M=1.05~{\rm g\,cm^{-3}}$ corresponds to the value in Fig. 6(b), for which the percolated free volume decreases to zero for probe sizes of both 2.8 Å and 3.4 Å. For $\rho_M < 1.05$ g cm⁻³ the linear relation on the semi-log plot indicates that the water flux decreases exponentially with membrane density. This is likely related to the decrease in water accessible pores, essentially the percolated free volume, with increasing membrane density. Additionally, the general collapse of the data in Fig. 10(b) for a total of 220 independent simulations for a wide range of membrane models indicates the robust nature of the flux-density relation and the outstanding overall repeatability of these simulations.

3.4. Water dynamics: diffusion

Simultaneous with the advection of water due to the transmembrane pressure resulting in a net flux through the membrane, Brownian motion of water molecules occurs as they interact with each other and the membrane nanostructure. Thus, to further understand the motion of water during transport, we examine the diffusivity of water within all the charged membrane models. The mean square displacement (MSD) provides an approach of analyzing the nature of the motion of water molecules inside and outside the membrane. The MSD is calculated as [74–79]:

$$MSD(\tau) = \left\langle \overline{\Delta r^2(t,\tau)} \right\rangle = \frac{1}{N} \sum_{i=1}^{N} \overline{[r_i(t+\tau) - r_i(t) - V_d \tau]^2}$$
 (1)

where τ is the time interval, Δr is the displacement of a water molecule, $\langle . \rangle$ indicates the expected value for the ensemble of N molecules, the overbar represents the average over time, r_i is the three-dimensional vector location of water molecule i, t is time, and V_d is the drift velocity, which is proportional to the water flux (essentially, the net flow in the z-direction for the membranes considered here). V_d in the membrane is based on the average z-component of velocity of water molecules in the membrane, and V_d in the reservoir is directly calculated from the motion of the graphene sheets. Thus, the MSD is essentially the square of the fluctuations in the location of molecules in time τ on average, apart from their displacement due to transport across the membrane. We have separately considered the diffusion in the transport direction (z) and in the transverse (x and y) directions; the corresponding MSD values do not differ significantly from each other. Based on Einstein's 1905 paper on the theory of diffusion [80], the MSD can be related to the diffusion coefficient D for Brownian motion, which can be expressed in a general form as [74,76,77,81,82]

$$MSD(\tau) = 2 n D \tau^{\alpha}$$
 (2)

where n is the number of dimensions for the motion of the molecules (n=3) in this case), and α characterizes the diffusivity [75,77,81,82]. $\alpha=1$, equivalent to a linear relation between MSD and τ , corresponds to Brownian, or normal, diffusion in which motion is dominated by collisions so that molecules follow a random walk. For $0<\alpha<1$, the motion of molecules is sub-diffusive, which results from a situation in which molecules are hindered or "caged" in some way. For $1<\alpha<2$, the diffusion is enhanced by molecule transport. Accounting for the drift velocity in the equation for the MSD eliminates such molecule transport for the situation considered here. For $\alpha=2$, the motion is ballistic in which molecules move freely with no collisions after an initial impulse [74], a condition which occurs at time intervals and displacements much smaller than those considered here. It is useful to take the logarithm of both sides of Eq. (2) to express it as:

$$\log(MSD) = \log(2nD) + \alpha \log(\tau)$$
 (3)

This form, equivalent to plotting MSD versus time interval τ on a log–log plot allows the easy visual comparison of D and α for different conditions [77]. Large D corresponds to large values of MSD, and the slope of the relation indicates the value of α and, hence, the nature of the diffusion.

With this context, the MSD is calculated for time intervals τ ranging from 2 ps (the highest resolution of water trajectories) to 1 ns for all the charged membranes. Water trajectories obtained from NEMD simulations are divided into three categories: bulk water away from the membrane interfaces regardless of the type of membrane (loose or dense), permeated water (excluding water molecules trapped in closed pores or confined space in the membrane) while traversing in the active portion of loose charged membranes, and permeated water traversing in the active portion of dense charged membranes. Among all NEMD simulations and within each category, MSD is calculated for each water molecule and averaged over the total number of water molecules in

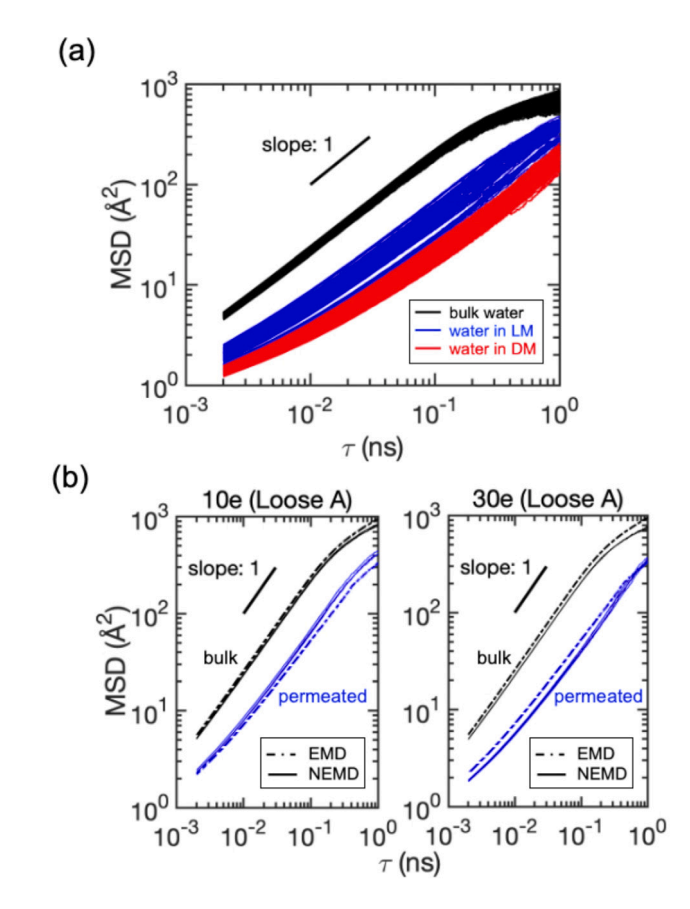


Fig. 12. (a) MSD vs. time interval for bulk water (black, 128 simulations) outside of 32 charged membranes, permeated water inside 16 loose charged membranes (LM, blue, 64 simulations), and permeated water inside 16 dense charged membranes (DM, red, 64 simulations) measured during the 20-ns NEMD simulations. (b) MSD vs. time interval for two example membranes showing bulk water (black) and permeated water (blue) within four 20-ns NEMD simulations (solid curves) and one 100-ns EMD simulation (dash-dotted curves). (Color online.).

each of the samples. Thus, each of the overlapping curves shown in Fig. 12(a) represents the average MSD for 283 to 2645 water molecules for one charged membrane realization. The overlapping curves of each color demonstrate the range of results in each of the three categories. Among three groups, bulk water (black curves) has the highest MSD values and, consequently, the highest diffusion coefficient at any given τ as the water on either side of the membrane is free of confinement. Water inside loose membranes (blue curves) is less mobile, as suggested by the lower MSD values, and water molecules inside dense membranes (red curves) have the least mobility with even lower MSD values. The spread of MSD curves for bulk water is quite narrow, demonstrating the robust nature of the calculations. However, the water mobility within the membrane depends on the membrane structure and membrane charge, as indicated by the larger spreads in their MSD curves. Similar MSD results obtained for neutral membranes generally overlay the charged ones (see Fig. S3 in the supplementary material).

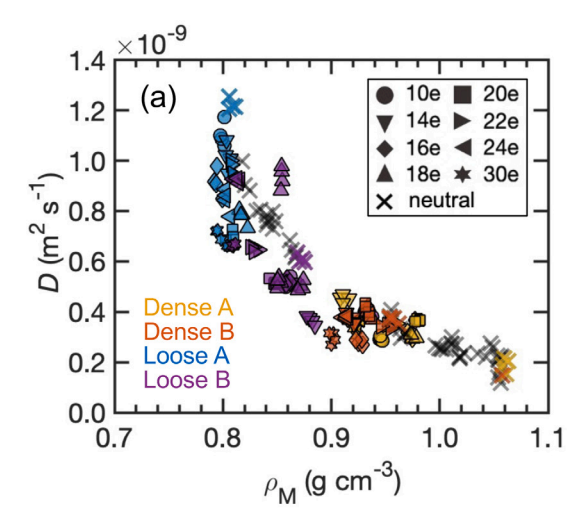
The nature of the diffusion for each water category can be determined based on the MSD curves. Bulk water exhibits normal diffusive behavior ($\tau < 0.1$ ns), as indicated by the slope of approximately one (0.87 $\leq \alpha \leq$ 0.92), consistent with more detailed measurements giving $\alpha = 0.92$ for water [74]. The reduced slope at large values of τ reflects the constraint of the overall system size, which is on the order of 20 Šfor each reservoir, corresponding to a MSD on the order of 400 Ų where the slope starts to deviate from $\alpha \sim 1$. Similarly, the slope of the MSD for water inside the membranes changes at small values of τ , consistent with the approximate membrane pore size, which is on the order of

3 Å (Fig. 4), corresponding to a MSD on the order of 10 Å^2 . Thus, the diffusion of water inside the membrane is sub-diffusive (0.58 $\leq \alpha \leq$ 0.82) when τ is less than about 0.03 ns, reflecting the constraint of water molecule motion in the membrane pores. At short enough time intervals, τ , and corresponding values of MSD, we would expect the MSD curves for the membranes should converge with those for bulk water, because at the scales of the membrane pores, the motion of the water molecules is not constrained. However, this requires a much smaller output time resolution than 2 ps per frame used in this study. At the other end of the time interval range, when τ is between 0.03 ns and 1 ns, α ranges from 0.78 to 0.99 inside the membranes, indicating that the diffusive nature of water in both the loose and dense membranes approaches that for water outside of the membrane (α slightly less than 1) because of the random walk nature of water molecules interacting with the membrane structure at larger time scales.

Before considering the diffusion coefficient derived from the MSD data, it is useful to examine the effect of the transmembrane pressure on water self-diffusion. To do this, we consider two membranes, 10e and 30e from the Loose A group, as examples and applied 0.1 MPa on both sides of the membrane to render a system without pressure difference. Since no transmembrane pressure is introduced, these are EMD systems, which are performed for 100 ns to obtain statistically meaningful results. For both membranes, the water flux is essentially zero. However, as illustrated in Fig. 12(b), there is no significant difference between the MSD curves for the EMD and NEMD simulations within the range of τ considered. Therefore, transmembrane pressure and the subsequent water flux do not have any significant impact on water diffusivity. It is the pressure difference across the membrane that provides directionality for water transport and facilitates permeation through the membrane. Diffusivity is related to the mobility of water, which is prescribed by the membrane porosity, and is unrelated to the applied transmembrane pressure.

To quantify the diffusion coefficient D, we consider the bulk water activity and water permeation in the range of time intervals where it can be considered as essentially normal diffusion ($\alpha \approx 1$). The dependence of the diffusion coefficient extracted from each water transport simulation on the membrane density ρ_M and the water flux are shown in Fig. 13(a) and (b), respectively. As would be expected based on the constraining effect of the membrane structure on water molecule motion, D decreases as ρ_M increases (Fig. 13(a)). The decrease is sharpest for low-density membranes and is less dramatic as ρ_M gets larger. The number water flux and *D* are linearly correlated (Fig. 13(b)). This is not surprising. High diffusivity is associated with low membrane density (Fig. 13(a)) because the membrane constrains the motion of water molecules less than in a more dense membrane. Likewise, high water flux is associated with low membrane density (Fig. 10(b)), again because the membrane constrains the motion of water molecules less than in a more dense membrane. Since both water diffusivity in the membrane and water flux through the membrane depend similarly on the membrane density, it is reasonable that the two quantities are directly correlated with each other, as is clearly evident in Fig. 13(b).

Finally, to confirm and validate our results, we compare the values we measure for D in bulk water and water inside membrane with both experimental and other MD studies. Here, D for bulk water is calculated to be $3.64 \pm 0.12 \times 10^{-9} \mathrm{m}^2 \ \mathrm{s}^{-1}$, which is in reasonable agreement with experimental results of $2.23 - 2.32 \times 10^{-9} \mathrm{m}^2 \ \mathrm{s}^{-1}$ [20,83–87] measured at 298 K. When considering bulk water self-diffusivities based on theoretical studies and MD simulations, there is considerably more variation, in the range of $2.0 - 6.3 \times 10^{-9} \ \mathrm{m}^2 \ \mathrm{s}^{-1}$ [61,74,88–92]. In previous studies, both the TIP3P and the modified TIP3P models tend to have higher diffusivities than the experimental data at the same temperature, and our value of $3.64 \pm 0.12 \times 10^{-9} \ \mathrm{m}^2 \ \mathrm{s}^{-1}$ is consistent with these previous MD simulation results. We find D for water inside membrane models to be $0.27 - 1.22 \times 10^{-9} \ \mathrm{m}^2 \ \mathrm{s}^{-1}$, which is somewhat higher than the values of $0.15 \pm 0.03 \times 10^{-9} \ \mathrm{m}^2 \ \mathrm{s}^{-1}$ measured in a RO membrane having a membrane density of $1.20 \ \mathrm{g \, cm}^{-3}$ [84]. This is not



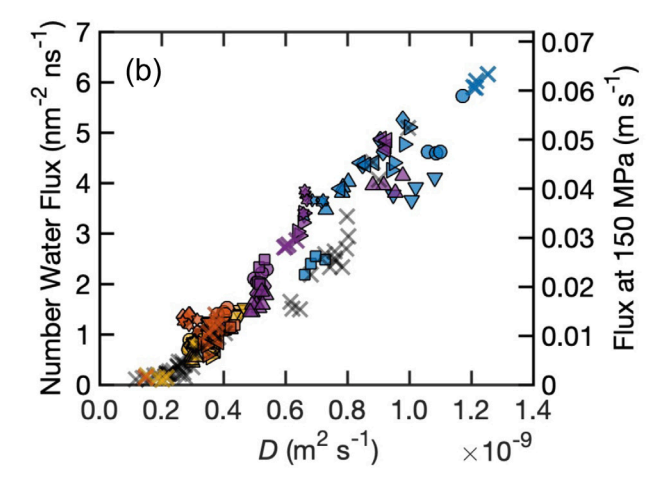


Fig. 13. (a) Diffusion coefficients D as a function of membrane density ρ_M and (b) the correlation between number water flux and diffusion coefficients D. Neutral membranes are shown as "×" where 4 sets of neutral membranes have matching colors with their corresponding charged membranes and the rest are shown in black. Data for a total of 220 simulations is shown. (Color online.).

surprising, given that RO membranes are typically more dense than NF membranes, likely resulting in a lower value of D. In fact, although the horizontal scale in Fig. 13(a) does not extend to membrane densities as high as $\rho_M=1.2~{\rm g\,cm^{-3}}$, it appears that this data for this RO membrane would be consistent with the dependence of D on ρ_M in this figure. In theoretical studies and MD simulations, D in RO membranes has been found to be around 0.14– $0.80\times10^{-9}~{\rm m^2~s^{-1}}$ [20,21,61,88], which is close to the values measured for D for dense membranes and some loose membranes here.

It is evident that membrane charge does not directly influence water transport activity or diffusion, as indicated in Fig. 13(b). Instead, it is the effect of the membrane local structure, quantified here in terms of membrane density ρ_M , which may be affected by the membrane charge, that governs water flux and diffusion.

4. Conclusions

Although NF membranes are routinely used in wide variety of water applications, charge interactions in these membranes are poorly understood at the atomic scale. Here we begin to address this by using molecular dynamics to explore 56 neutral and charged PIP-based NF membrane models, conducting a total of 220 NEMD simulations and 57 EMD simulations. This large number of simulations allows us to

characterize these NF models over a wide range of membrane densities and charge concentrations to uncover the relationship between NF physical properties and water dynamics.

The membrane models considered here have realistic elemental composition, physical properties, and water transport performance compared to actual PIP-based FilmTec™ NF270 membranes based on the characterization of membrane-only density ρ_M (Fig. 3), pore size (Figs. 4 and 5), free volume (Fig. 6), and water flux (Fig. 10). For the negatively charged membrane models, the number of negatively charged carboxylate groups, which corresponds to increasing pH, has a minor effect on the membrane structure, the degree of which varies from one membrane model to another. Although there is a slight tendency for the membrane to swell with increasing charge, the membrane density is not monotonically related to the membrane charge (Fig. 8). Consequently, the membrane charge concentration does not directly affect water flux (Fig. 10(a)). Instead, the water flux depends nearly entirely on the membrane density. The presence of charged carboxylate groups and sodium counterions within the membrane tends to swell the membrane structure and increase water accessible free volume, which can reduce the membrane density and thereby affect the transport properties by increasing the water flux (Fig. 10(b)). This effect is most evident in membrane models with relatively high densities where charges are in close proximity. At low membrane densities ($\rho_M \leq$ 0.82 g cm⁻³), however, the membrane can be so loose that the water flux is not strongly correlated with the membrane density.

The membrane density, which of course can be altered by the membrane charge along with counterions in the membrane, also determines the diffusion of water within the membrane structure (Fig. 13(a)). Thus, water diffusivity, a metric indicative of water mobility inside the membrane, depends on the membrane structure, quantified here in terms of the membrane density. Since both water flux and water diffusivity are determined by the membrane structure, water flux and water diffusivity themselves are correlated with each other (Fig. 13(b)). It is important to note that high water flux is not a consequence of high water diffusivity; instead both are related to a loose membrane structure corresponding to low membrane density. It is also important to note that the diffusion coefficients are independent of the transmembrane pressure. Diffusion corresponds to the random walk trajectories taken by the water molecules, which are also influenced by the presence of the non-equilibrium transmembrane pressure resulting in a net transport through the membrane. Thus, water transport through the membrane can be seen as a random walk with transmembrane pressure controlling the direction and magnitude of the net water molecule movement.

This study provides the foundation for further studies on charged PIP-based NF membranes by illuminating the effect of charge on the membrane structure and basic water transport properties. Furthermore, the approaches for modeling membrane charge used here can also be extended to simulations of other charged membranes including MPD-based RO membranes. However, there are still questions left unanswered such as how local membrane conformation is related to the membrane charge, how the membrane charge affects the transport of ionic solutes of different valencies, and how the ionic solutes in the feed influence water transport. In subsequent work, we intend to focus on membrane—ion and ion—ion interactions in charged NF membranes in order to broaden the application of this important class of membranes.

CRediT authorship contribution statement

Suwei Liu: Conceptualization, Methodology, Software, Validation, Visualization, Investigation, Data curation, Writing - original draft. Saahir Ganti-Agrawal: Investigation, Data curation, Writing - original draft. Sinan Keten: Writing - Reviewing and editing, Supervision. Richard M. Lueptow: Writing - Reviewing and editing, Supervision, Funding Acquisition.

Declaration of competing interest

The authors declare that they have no known competing financial interests or personal relationships that could have appeared to influence the work reported in this paper.

Acknowledgments

Suwei Liu thanks Dr. Steven Jons, Dr. Toni Bechtel, and Dr. Jeffrey Wilbur from DuPont de Nemours, Inc for several helpful discussions.

Funding

This research was sponsored by a grant from the National Science Foundation, USA (Grant No.: CBET-1840816).

Appendix A. Supplementary data

Supplementary material related to this article can be found online at https://doi.org/10.1016/j.memsci.2021.120057.

References

- [1] Y. Kiso, Y. Sugiura, T. Kitao, K. Nishimura, Effects of hydrophobicity and molecular size on rejection of aromatic pesticides with nanofiltration membranes, J. Membr. Sci. 192 (1–2) (2001) 1–10.
- [2] A. Schäfer, L. Nghiem, T. Waite, Removal of the natural hormone estrone from aqueous solutions using nanofiltration and reverse osmosis, Environ. Sci. Technol. 37 (1) (2003) 182–188.
- [3] Y. Kiso, Y. Nishimura, T. Kitao, K. Nishimura, Rejection properties of nonphenylic pesticides with nanofiltration membranes, J. Membr. Sci. 171 (2) (2000) 229–237.
- [4] Y. Yoon, R.M. Lueptow, Removal of organic contaminants by RO and NF membranes, J. Membr. Sci. 261 (1–2) (2005) 76–86.
- [5] T. Uemura, M. Henmi, Thin-film composite membranes for reverse osmosis, in: Advanced Membrane Technology and Applications, Wiley Online Library, 2008, pp. 1–19.
- [6] M. Pontié, H. Dach, J. Leparc, M. Hafsi, A. Lhassani, Novel approach combining physico-chemical characterizations and mass transfer modelling of nanofiltration and low pressure reverse osmosis membranes for brackish water desalination intensification, Desalination 221 (1–3) (2008) 174–191.
- [7] S. Lee, R.M. Lueptow, Reverse osmosis filtration for space mission wastewater: Membrane properties and operating conditions, J. Membr. Sci. 182 (1–2) (2001) 77–90
- [8] L.Y. Ng, A.W. Mohammad, C.Y. Ng, C.P. Leo, R. Rohani, Development of nanofiltration membrane with high salt selectivity and performance stability using polyelectrolyte multilayers, Desalination 351 (2014) 19–26.
- [9] O. Labban, C. Liu, T.H. Chong, J.H. Lienhard, Relating transport modeling to nanofiltration membrane fabrication: Navigating the permeability-selectivity trade-off in desalination pretreatment, J. Membr. Sci. 554 (2018) 26–38.
- [10] N.L. Le, S.P. Nunes, Materials and membrane technologies for water and energy sustainability, Sustain. Mater. Technol. 7 (2016) 1–28.
- [11] R.J. Petersen, Composite reverse osmosis and nanofiltration membranes, J. Membr. Sci. 83 (1) (1993) 81–150.
- [12] V. Freger, Nanoscale heterogeneity of polyamide membranes formed by interfacial polymerization, Langmuir 19 (11) (2003) 4791–4797.
- [13] S.D. Arthur, Structure-property relationship in a thin film composite reverse osmosis membrane, J. Membr. Sci. 46 (2–3) (1989) 243–260.
- [14] G.-Y. Chai, W.B. Krantz, Formation and characterization of polyamide membranes via interfacial polymerization, J. Membr. Sci. 93 (2) (1994) 175–192.
 [15] D.G. Cahill, V. Freger, S.-Y. Kwak, Microscopy and microanalysis of
- reverse-osmosis and nanofiltration membranes, MRS Bull. 33 (1) (2008) 27–32. [16] O. Coronell, B.J. Marinas, D.G. Cahill, Depth heterogeneity of fully aromatic
- [16] O. Coronell, B.J. Marinas, D.G. Cahill, Depth heterogeneity of fully aromatic polyamide active layers in reverse osmosis and nanofiltration membranes, Environ. Sci. Technol. 45 (10) (2011) 4513–4520.
- [17] J.G. Wijmans, R.W. Baker, The solution-diffusion model: A unified approach to membrane permeation, Materials Science of Membranes for Gas and Vapor Separation, vol. 1, John Wiley & Sons, Ltd., Hoboken, NJ, USA, 2006, pp. 159-189
- [18] W. Bowen, A.W. Mohammad, Characterization and prediction of nanofiltration membrane performance—A general assessment, Chem. Eng. Res. Des. 76 (8) (1998) 885–893.
- [19] M. Kotelyanskii, N. Wagner, M. Paulaitis, Molecular dynamics simulation study of the mechanisms of water diffusion in a hydrated, amorphous polyamide, Comput. Theor. Polym. Sci. 9 (3–4) (1999) 301–306.

- [20] E. Harder, D.E. Walters, Y.D. Bodnar, R.S. Faibish, B. Roux, Molecular dynamics study of a polymeric reverse osmosis membrane, J. Phys. Chem. B 113 (30) (2009) 10177–10182.
- [21] Z.E. Hughes, J.D. Gale, A computational investigation of the properties of a reverse osmosis membrane. J. Mater. Chem. 20 (36) (2010) 7788–7799.
- [22] Y. Luo, E. Harder, R.S. Faibish, B. Roux, Computer simulations of water flux and salt permeability of the reverse osmosis FT-30 aromatic polyamide membrane, J. Membr. Sci. 384 (1–2) (2011) 1–9.
- [23] M. Ding, A. Szymczyk, F. Goujon, A. Soldera, A. Ghoufi, Structure and dynamics of water confined in a polyamide reverse-osmosis membrane: A molecular-simulation study, J. Membr. Sci. 458 (2014) 236–244.
- [24] V. Kolev, V. Freger, Hydration, porosity and water dynamics in the polyamide layer of reverse osmosis membranes: A molecular dynamics study, Polymer 55 (6) (2014) 1420–1426.
- [25] V. Kolev, V. Freger, Molecular dynamics investigation of ion sorption and permeation in desalination membranes, J. Phys. Chem. B 119 (44) (2015) 14168-14179
- [26] M. Shen, S. Keten, R.M. Lueptow, Rejection mechanisms for contaminants in polyamide reverse osmosis membranes, J. Membr. Sci. 509 (2016) 36–47.
- [27] M. Shen, S. Keten, R.M. Lueptow, Dynamics of water and solute transport in polymeric reverse osmosis membranes via molecular dynamics simulations, J. Membr. Sci. 506 (2016) 95–108.
- [28] H. Zhang, M.S. Wu, K. Zhou, A.W.-K. Law, Molecular insights into the composition–structure–property relationships of polyamide thin films for reverse osmosis desalination, Environ. Sci. Technol. 53 (11) (2019) 6374–6382.
- [29] M. Paul, S.D. Jons, Chemistry and fabrication of polymeric nanofiltration membranes: A review, Polymer 103 (2016) 417–456.
- [30] R. Epsztein, E. Shaulsky, N. Dizge, D.M. Warsinger, M. Elimelech, Role of ionic charge density in donnan exclusion of monovalent anions by nanofiltration, Environ. Sci. Technol. 52 (7) (2018) 4108–4116.
- [31] C. Bellona, J.E. Drewes, The role of membrane surface charge and solute physicochemical properties in the rejection of organic acids by NF membranes, J. Membr. Sci. 249 (1–2) (2005) 227–234.
- [32] P. Xu, J.E. Drewes, C. Bellona, G. Amy, T.-U. Kim, M. Adam, T. Heberer, Rejection of emerging organic micropollutants in nanofiltration-reverse osmosis membrane applications, Water Environ. Res. 77 (1) (2005) 40-48.
- [33] K. Li, S. Li, L. Liu, W. Huang, Y. Wang, C. Yu, Y. Zhou, Molecular dynamics simulation studies of the structure and antifouling performance of a gradient polyamide membrane. Phys. Chem. Chem. Phys. 21 (36) (2019) 19995–20002.
- [34] T.E. Culp, B. Khara, K.P. Brickey, M. Geitner, T.J. Zimudzi, J.D. Wilbur, S.D. Jons, A. Roy, M. Paul, B. Ganapathysubramanian, et al., Nanoscale control of internal inhomogeneity enhances water transport in desalination membranes, Science 371 (6524) (2021) 72–75.
- [35] O. Coronell, B.J. Mariñas, X. Zhang, D.G. Cahill, Quantification of functional groups and modeling of their ionization behavior in the active layer of FT30 reverse osmosis membrane, Environ. Sci. Technol. 42 (14) (2008) 5260–5266.
- [36] A. Schäfer, A.G. Fane, T.D. Waite, Nanofiltration: Principles and Applications, Elsevier, 2005.
- [37] A.P. Rao, N. Desai, R. Rangarajan, Interfacially synthesized thin film composite RO membranes for seawater desalination, J. Membr. Sci. 124 (2) (1997) 263–272.
- [38] K. Košutić, D. Dolar, D. Ašperger, B. Kunst, Removal of antibiotics from a model wastewater by RO/NF membranes, Sep. Purif. Technol. 53 (3) (2007) 244–249.
- [39] Z. Cui, Y. Jiang, R. Field, Fundamentals of pressure-driven membrane separation processes, in: Membrane Technology, Elsevier, 2010, pp. 1–18.
- [40] L. Naidu, S. Saravanan, M. Chidambaram, M. Goel, A. Das, J. Babu, Nanofiltration in transforming surface water into healthy water: Comparison with reverse osmosis, J. Chem. 2015 (2015).
- [41] J. Wang, R.M. Wolf, J.W. Caldwell, P.A. Kollman, D.A. Case, Development and testing of a general AMBER force field, J. Comput. Chem. 25 (9) (2004) 1157, 1174
- [42] A. Jakalian, D.B. Jack, C.I. Bayly, Fast, efficient generation of high-quality atomic charges. AM1-BCC model: II. Parameterization and validation, J. Comput. Chem. 23 (16) (2002) 1623–1641.
- [43] J. Wang, W. Wang, P.A. Kollman, D.A. Case, Automatic atom type and bond type perception in molecular mechanical calculations, J. Mol. Graph. 25 (2) (2006) 247–260.
- [44] J.R. Gissinger, B.D. Jensen, K.E. Wise, Modeling chemical reactions in classical molecular dynamics simulations, Polymer 128 (2017) 211–217.
- [45] S. Plimpton, Fast parallel algorithms for short-range molecular dynamics, J. Comput. Phys. 117 (1) (1995) 1–19.
- [46] O. Coronell, M.I. González, B.J. Mariñas, D.G. Cahill, Ionization behavior, stoichiometry of association, and accessibility of functional groups in the active layers of reverse osmosis and nanofiltration membranes, Environ. Sci. Technol. 44 (17) (2010) 6808–6814.
- [47] J.C. Phillips, R. Braun, W. Wang, J. Gumbart, E. Tajkhorshid, E. Villa, C. Chipot, R.D. Skeel, L. Kale, K. Schulten, Scalable molecular dynamics with NAMD, J. Comput. Chem. 26 (16) (2005) 1781–1802.
- [48] J.-P. Ryckaert, G. Ciccotti, H.J. Berendsen, Numerical integration of the Cartesian equations of motion of a system with constraints: Molecular dynamics of n-alkanes, J. Comput. Phys. 23 (3) (1977) 327–341.

- [49] T. Darden, D. York, L. Pedersen, Particle mesh Ewald: An N · log(N) method for Ewald sums in large systems, J. Chem. Phys. 98 (12) (1993) 10089–10092.
- [50] O. Coronell, B. Mi, B.J. Mariña, D.G. Cahill, Modeling the effect of charge density in the active layers of reverse osmosis and nanofiltration membranes on the rejection of arsenic (III) and potassium iodide, Environ. Sci. Technol. 47 (1) (2013) 420–428.
- [51] S. Karan, Z. Jiang, A.G. Livingston, Sub-10 nm polyamide nanofilms with ultrafast solvent transport for molecular separation, Science 348 (6241) (2015) 1347-1351.
- [52] A.S. Gorzalski, C. Donley, O. Coronell, Elemental composition of membrane foulant layers using EDS, XPS, and RBS, J. Membr. Sci. 522 (2017) 31–44.
- [53] J. Tanninen, M. Mänttäri, M. Nyström, Effect of salt mixture concentration on fractionation with NF membranes, J. Membr. Sci. 283 (1–2) (2006) 57–64.
- [54] W. Humphrey, A. Dalke, K. Schulten, VMD: Visual molecular dynamics, J. Mol. Graph. 14 (1) (1996) 33–38.
- [55] W.L. Jorgensen, J. Chandrasekhar, J.D. Madura, R.W. Impey, M.L. Klein, Comparison of simple potential functions for simulating liquid water, J. Chem. Phys. 79 (2) (1983) 926–935.
- [56] D. Beglov, B. Roux, Finite representation of an infinite bulk system: Solvent boundary potential for computer simulations, J. Chem. Phys. 100 (12) (1994) 9050–9063.
- [57] E. Dražević, K. Košutić, V. Freger, Permeability and selectivity of reverse osmosis membranes: Correlation to swelling revisited, Water Res. 49 (2014) 444–452.
- [58] F. Pacheco, R. Sougrat, M. Reinhard, J.O. Leckie, I. Pinnau, 3D visualization of the internal nanostructure of polyamide thin films in RO membranes, J. Membr. Sci. 501 (2016) 33–44.
- [59] S. Gumma, O. Talu, Gibbs dividing surface and helium adsorption, Adsorption 9 (1) (2003) 17–28.
- [60] B. Mi, D.G. Cahill, B.J. Mariñas, Physico-chemical integrity of nanofiltration/reverse osmosis membranes during characterization by rutherford backscattering spectrometry, J. Membr. Sci. 291 (1–2) (2007) 77–85.
- [61] X. Zhang, D.G. Cahill, O. Coronell, B.J. Mariñas, Absorption of water in the active layer of reverse osmosis membranes, J. Membr. Sci. 331 (1–2) (2009) 143–151.
- [62] L. Sarkisov, R. Bueno-Perez, M. Sutharson, D. Fairen-Jimenez, Materials informatics with PoreBlazer v4.0 and the CSD MOF database, Chem. Mater. 32 (23) (2020) 9849–9867.
- [63] N. Hilal, H. Al-Zoubi, N. Darwish, A. Mohamma, M.A. Arabi, A comprehensive review of nanofiltration membranes: Treatment, pretreatment, modelling, and atomic force microscopy, Desalination 170 (3) (2004) 281–308.
- [64] M. Gerstein, C. Chothia, Packing at the protein-water interface, Proc. Natl. Acad. Sci. 93 (19) (1996) 10167–10172.
- [65] A.-J. Li, R. Nussinov, A set of van der Waals and coulombic radii of protein atoms for molecular and solvent-accessible surface calculation, packing evaluation, and docking, Proteins Struct. Funct. Bioinform. 32 (1) (1998) 111–127.
- [66] S.H. Kim, S.-Y. Kwak, T. Suzuki, Positron annihilation spectroscopic evidence to demonstrate the flux-enhancement mechanism in morphology-controlled thin-film-composite (TFC) membrane, Environ. Sci. Technol. 39 (6) (2005) 1764–1770.
- [67] H.Q. Dang, W.E. Price, L.D. Nghiem, The effects of feed solution temperature on pore size and trace organic contaminant rejection by the nanofiltration membrane NF270, Sep. Purif. Technol. 125 (2014) 43–51.
- [68] S. Lee, R.M. Lueptow, Membrane rejection of nitrogen compounds, Environ. Sci. Technol. 35 (14) (2001) 3008–3018.
- [69] H.F. Ridgway, J. Orbell, S. Gray, Molecular simulations of polyamide membrane materials used in desalination and water reuse applications: Recent developments and future prospects, J. Membr. Sci. 524 (2017) 436–448.
- [70] M. Kotelyanskii, N. Wagner, M. Paulaitis, Atomistic simulation of water and salt transport in the reverse osmosis membrane FT-30, J. Membr. Sci. 139 (1) (1998) 1–16.
- [71] L. Ruiz, Y. Wu, S. Keten, Tailoring the water structure and transport in nanotubes with tunable interiors, Nanoscale 7 (1) (2015) 121–132.
- [72] V. Freger, Swelling and morphology of the skin layer of polyamide composite membranes: An atomic force microscopy study, Environ. Sci. Technol. 38 (11) (2004) 3168–3175.
- [73] J. Ji, M. Mehta, Mathematical model for the formation of thin-film composite hollow fiber and tubular membranes by interfacial polymerization, J. Membr. Sci. 192 (1–2) (2001) 41–54.
- [74] M. Riahi, I. Qattan, J. Hassan, D. Homouz, Identifying short-and long-time modes of the mean-square displacement: An improved nonlinear fitting approach, AIP Adv. 9 (5) (2019) 055112.
- [75] R. Metzler, J.-H. Jeon, A.G. Cherstvy, E. Barkai, Anomalous diffusion models and their properties: Non-stationarity, non-ergodicity, and ageing at the centenary of single particle tracking, Phys. Chem. Chem. Phys. 16 (44) (2014) 24128–24164.
- [76] T. Li, M.G. Raizen, Brownian motion at short time scales, Ann. Phys. 525 (4) (2013) 281–295.
- [77] E. Kepten, A. Weron, G. Sikora, K. Burnecki, Y. Garini, Guidelines for the fitting of anomalous diffusion mean square displacement graphs from single particle tracking experiments, PLoS One 10 (2) (2015) e0117722.
- [78] Y. Fan, P.B. Umbanhowar, J.M. Ottino, R.M. Lueptow, Shear-rate-independent diffusion in granular flows, Phys. Rev. Lett. 115 (8) (2015) 088001.

- [79] A.M. Fry, P.B. Umbanhowar, J.M. Ottino, R.M. Lueptow, Diffusion, mixing, and segregation in confined granular flows, AIChE J. 65 (3) (2019) 875–881.
- [80] A. Einstein, On the motion of small particles suspended in liquids at rest required by the molecular-kinetic theory of heat, Ann. Phys. 17 (549–560) (1905) 208.
- [81] M.J. Saxton, K. Jacobson, Single-particle tracking: Applications to membrane dynamics, Annu. Rev. Biophys. Biomol. Struct. 26 (1) (1997) 373–399.
- [82] N. Ruthardt, D.C. Lamb, C. Bräuchle, Single-particle tracking as a quantitative microscopy-based approach to unravel cell entry mechanisms of viruses and pharmaceutical nanoparticles, Mol. Ther. 19 (7) (2011) 1199–1211.
- [83] A.J. Easteal, W.E. Price, L.A. Woolf, Diaphragm cell for high-temperature diffusion measurements. Tracer diffusion coefficients for water to 363 k, J. Chem. Soc. Faraday Trans. 1 Phys. Chem. Condens. Phases 85 (5) (1989) 1091–1097.
- [84] M. Frommer, J. Murday, R. Messalem, Solubility and diffusivity of water and of salts in an aromatic polyamide film, Eur. Polym. J. 9 (4) (1973) 367–373.
- [85] K.T. Gillen, D. Douglass, M. Hoch, Self-diffusion in liquid water to -31°C, J. Chem. Phys. 57 (12) (1972) 5117–5119.

- [86] K.R. Harris, L.A. Woolf, Pressure and temperature dependence of the self diffusion coefficient of water and oxygen-18 water, J. Chem. Soc. Faraday Trans. 1 Phys. Chem. Condens. Phases 76 (1980) 377–385.
- [87] M. Holz, S.R. Heil, A. Sacco, Temperature-dependent self-diffusion coefficients of water and six selected molecular liquids for calibration in accurate ¹H NMR PFG measurements, Phys. Chem. Chem. Phys. 2 (20) (2000) 4740–4742.
- [88] M. Ding, A. Ghoufi, A. Szymczyk, Molecular simulations of polyamide reverse osmosis membranes, Desalination 343 (2014) 48–53.
- [89] V.A. Makarov, M. Feig, B.K. Andrews, B.M. Pettitt, Diffusion of solvent around biomolecular solutes: A molecular dynamics simulation study, Biophys. J. 75 (1) (1998) 150-158
- [90] P. Mark, L. Nilsson, Structure and dynamics of the TIP3P, SPC, and SPC/E water models at 298 K, J. Phys. Chem. A 105 (43) (2001) 9954–9960.
- [91] R. Mills, Self-diffusion in normal and heavy water in the range 1-45°, J. Phys. Chem. 77 (5) (1973) 685–688.
- [92] D.J. Price, C.L. Brooks III, A modified TIP3P water potential for simulation with ewald summation, J. Chem. Phys. 121 (20) (2004) 10096–10103.